The directional properties of wind waves from equilibrium to gravity-capillary scales

Nathan J. M. Laxague,[a,b] Zeynep Göksu Duvarcı,[b] Jan-Victor Björkqvist,[c]
Junzhe (Jerry) Liu,[d] Lindsay Hogan,[d]
Alejandro Cifuentes-Lorenzen,[e] and Christopher J. Zappa[d]

[a] *Department of Mechanical Engineering, University of New Hampshire, Durham, New Hampshire, USA*
[b] *Center for Ocean Engineering, University of New Hampshire, Durham, New Hampshire, USA*
[c] *Norwegian Meteorological Institute, Bergen, Norway*
[d] *Lamont-Doherty Earth Observatory of Columbia University, Palisades, New York, USA*
[e] *University of Connecticut, Groton, Connecticut, USA*

Corresponding author: Nathan J. M. Laxague, Nathan.Laxague@unh.edu

ABSTRACT: Ocean surface waves are perhaps the most prominent manifestation of the dynamical interaction between the earth's atmosphere and ocean. However, much of the available body of field observations of wind-generated surface waves is limited to longer waves (wavelengths of order 1 m and greater). Here we present recent results from a comprehensive field observational campaign aimed at describing the connection between the multiscale characteristics of wind-generated ocean surface waves and variation in air-sea momentum flux, long wave-wind misalignment, and near-surface current. We obtained directional wavenumber and frequency spectra from the equilibrium range through the gravity-capillary regime as well as direction-aware statistics of visible breaking waves. Misalignment between wind and long waves is found to be a key variable in wind wave directionality. We find that the very short wind waves (sub-decimeter short gravity and gravity-capillary waves) tend to propagate downwind on average and are not reliably affected by wind/long wave misalignment. However, misalignment between long waves and wind velocity is associated with off-wind propagation of waves in the equilibrium and saturation ranges (and the breaking fronts which accompany waves of those scales). This effect is smallest for young seas and increases with wave age. Finally, we observe that directional spreading is broadest at the upper extremum of the saturation range, beyond which (for short gravity and gravity-capillary waves) the spread narrows and the sea becomes unimodal in the downwind direction; this finding is consistent across all wave ages.

SIGNIFICANCE STATEMENT: Ocean surface waves are the quintessential expression of physical air-sea interaction. Their growth, development, and breaking is a crucial link in the coupled ocean-atmosphere system. Here we provide a comprehensive description of the directional characteristics of surface waves ranging from tens of meters to one centimeter in length. We find that when the wind is misaligned with long surface waves, intermediate waves and breakers are steered toward the long wave direction. This steering is not observed for the shortest wind waves or the near-surface current. We also find that wind wave directional spreading is broadest at those intermediate scales and narrow for the shortest wind waves, which tend to be tightly spread about a particular direction. These results provide clarity regarding the surface waves most responsive to local wind forcing.

1. Background & Motivation

As wind blows over the ocean, short waves grow, develop, and propagate downwind in response to the forcing. Complications to this development arise in myriad forms, including wave-wave interactions, wave-current interactions, wave breaking, and transience in the wind forcing itself. The end result is very much not straightforward: waves of different scales often exhibit radically different spreading behavior and are frequently misaligned in their mean propagation directions (Figure 1). Although each of these effects is complicated enough in its own right, considerable effort has been committed to understanding them in isolation—and, where feasible—in tandem. The surface waves which figure most prominently into the mediation of air-sea flux are sufficiently short and steep to modify the aerodynamic surface roughness (Makin et al. 1995). These are wind waves; the shortest and steepest of them are locally generated, so one might take as first-order assumptions that the mean wave direction is aligned with the wind direction and that wave directional spreading is symmetric about that direction. However, various factors (among them nonstationarity in wind forcing, wave-wave interaction, wave-current interaction, and depth-limited refraction) can modify the wave directional characteristics. These modifications yield a wave field that differs from the baseline, steady-state expectation for a given wind speed and fetch.

This deviation bears on processes larger in scale and broader in impact than the waves themselves. Drennan et al. (1999) demonstrated that the relative direction between wind and long waves has a substantial impact on the direction and magnitude of the wind stress. The misalignment between

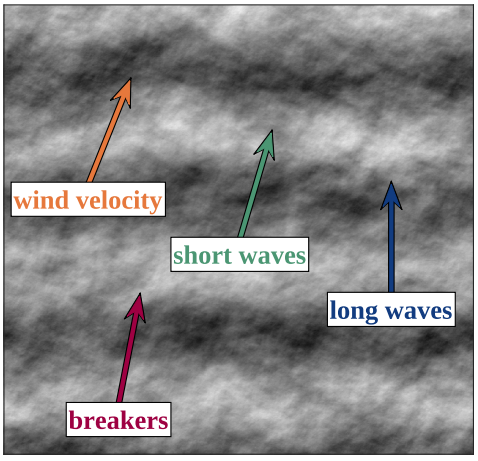

FIG. 1. Depiction of simulated sea state in which wind forcing may be misaligned with surface waves– e.g., long waves, wind waves (equilibrium range through capillary-scale), and breakers.

the wind and mean long wave directions is likely to result from spatiotemporally variable wind forcing or refraction of waves off the wind direction. The latter effect appears to be best-attributed to strong horizontal current gradients (Zhang et al. 2009) or propagation of waves into nearshore, shallow water environments (Potter et al. 2022). Large Eddy Simulations (LES) of turbulent wind blowing over monochromatic surface wave fields provide perhaps the most flexible means for investigating the question of wind-long wave interaction. Relative to a situation in which wind and waves are aligned, waves opposing wind will result in enhanced surface drag (Husain et al. 2022a), while waves moving obliquely ($\Delta\theta \approx 90^\circ \pm 45^\circ$) result in reduced surface drag (Husain et al. 2022b; Manzella et al. 2024). These results comport with the field observations of Drennan et al. (1999).

Despite this array of observations (and even larger array of modeling efforts), our understanding of the connection between wave directional properties and the turbulent stress in the atmospheric surface layer remains a point of relative weakness within air-sea interaction. In a recent review paper, Villas Bôas et al. (2019) noted that the modulation of the wind stress by surface waves was a "fundamental" problem within air-sea interaction– and that simultaneously obtaining directional wave spectra, near-surface currents, and wind stress will be essential to improving empirical parameterizations for air-sea fluxes. In their recent review of modeling and observational efforts, Ayet and Chapron (2022) came to the conclusion that there is an immediate need to make high-resolution (in space and time) observations of ocean surface wave characteristics in connection

with laboratory efforts in order to provide an improved understanding of the dynamical coupling between surface waves and atmospheric turbulence.

Perhaps some uncertainty is associated with our very own use of general terms like "long" and "short" when describing surface waves. "Swell" is appropriate in that its use demarcates the wave as being non-local and therefore much faster than might be expected for a wave in balance with the local wind forcing (and/or misaligned directionally with the wind). In conditions with very light wind forcing, there is even evidence of momentum flux from swell into the atmospheric boundary layer (Kahma et al. 2016). Investigations into the specific mechanisms responsible for the modulation of wind stress by surface waves are ongoing, with efforts made to be specific as possible about the scale of the waves being studied. Villarreal-Olavarrieta et al. (2024) argued that the presence of swell itself sets up a wave-coherent stress which may increase or decrease the observed wind stress depending on the swell / wind alignment. Ayet et al. (2020) used an analytical modeling framework to demonstrate that surface gravity waves of wavelength 10 m and longer directly modify the turbulent characteristics of the atmospheric surface layer. These modulations may also be driven by processes on the smaller side of things: waves in the equilibrium and saturation spectral subranges (Phillips 1985) are intimately connected to the local wind forcing (Banner 1990; Hara and Belcher 2002). These waves are "short" relative to swell (and indeed, on the shorter end of what can be reasonably measured with surface buoys). However, they respond slowly to changes in wind forcing and may exhibit persistent directional asymmetry in response to horizontal current gradients Tamura et al. (2008). The large sample size analysis of wind and wave measurements made at Ocean Station Papa (OSP) by Thomson et al. (2013) indicates that the mean wave direction within the equilibrium range is downwind, though a substantial amount of excursions were observed from that mean behavior.

Substantial developments have been made in our capabilities for observing the directional properties of waves in the equilibrium and saturation range. Airborne scanning LiDAR has been used to obtain observations of the ocean surface wave spectra on spatial scales ranging from 50 cm - 1 km (Lenain and Melville 2017). This encompasses the equilibrium range over all wind forcing conditions and may resolve the lower (longer) end of the saturation range for certain forcing conditions. Stereophotogrammetry provides a four-dimensional reconstruction of the ocean surface gravity wave field, typically for wave scales ranging from 100 m down to 50 cm (Benetazzo 2006;

Bergamasco et al. 2017). The wavenumber-frequency spectra (Leckler et al. 2015; Peureux et al. 2018) one may compute from stereo datasets offers rich information about wave propagation, directionality, and nonlinearity. However, surface waves shorter than those in the saturation range remain generally under-observed due to the substantial challenges associated with their measurement (Caulliez and Guérin 2012; Laxague et al. 2015). These waves are understood to support the majority of the momentum input to the wave field due to wind (Makin et al. 1995; Hwang 2005). This category of waves includes very short gravity waves (wavelengths ≈50 cm to ≈5 cm), gravity-capillary waves (wavelengths ≈5 cm to ≈5 mm), and pure capillary waves (wavelengths less than ≈5 mm); ranges are defined by the Bond number, the nondimensional balance between gravity and capillarity (Hager 2012).

Polarimetric Slope Sensing (PSS, Zappa et al. (2008)) was developed in order to address this observational need. There have been individual successful applications of the technique for making novel measurements of short wave spectra (Zappa et al. 2012; Laxague et al. 2015, 2018a), near-surface current (Laxague et al. 2017b, 2018b; Laxague and Zappa 2020b), and the response of short waves to rain (Laxague and Zappa 2020a) and chemical surfactants (Laxague et al. 2024). However, PSS has not yet been used to reliably describe the directionality of these short wind waves. In this paper we present the results of a field observational study designed to expand our understanding of the directional properties (i.e., including both mean direction and spreading/modality) of wind-generated ocean surface waves and the degree to which those properties are connected to variation in air-sea momentum flux, long wave-wind misalignment, and near-surface current. The present study was conducted with sufficient sample size ($N > 100$) to reasonably draw some general conclusions about the directional characteristics of waves in the equilibrium, saturation, short gravity, and gravity-capillary ranges. The campaign is described in section 2, with results presented in sections 3, 4, and 5. We discuss these results in the context of existing literature within section 6 and summarize our findings in 7.

2. Field Campaign

Between October 2019 and February 2020, an expansive set of measurements of physical air-sea interaction were made at the Air-Sea Interaction Tower (ASIT). ASIT is a rigid, low-profile structure located 3.2 km south of Martha's Vineyard along the 15 m isobath (Edson et al. 2007;

Denny et al. 2008). The location of the study site is shown in Figure 2, while a representation of the tower is provided in Figure 3b. ASIT was designed to allow for high-quality micrometeorological measurements to be made without the complications of platform motion or the contamination of airflow distortion, enabling long-duration process studies (Edson et al. 2007; Chang et al. 2025). ASIT is connected via fiber optic cable to a shore station on Martha's Vineyard that has power and internet connectivity, allowing for remote operation of high-bandwidth observational tools.

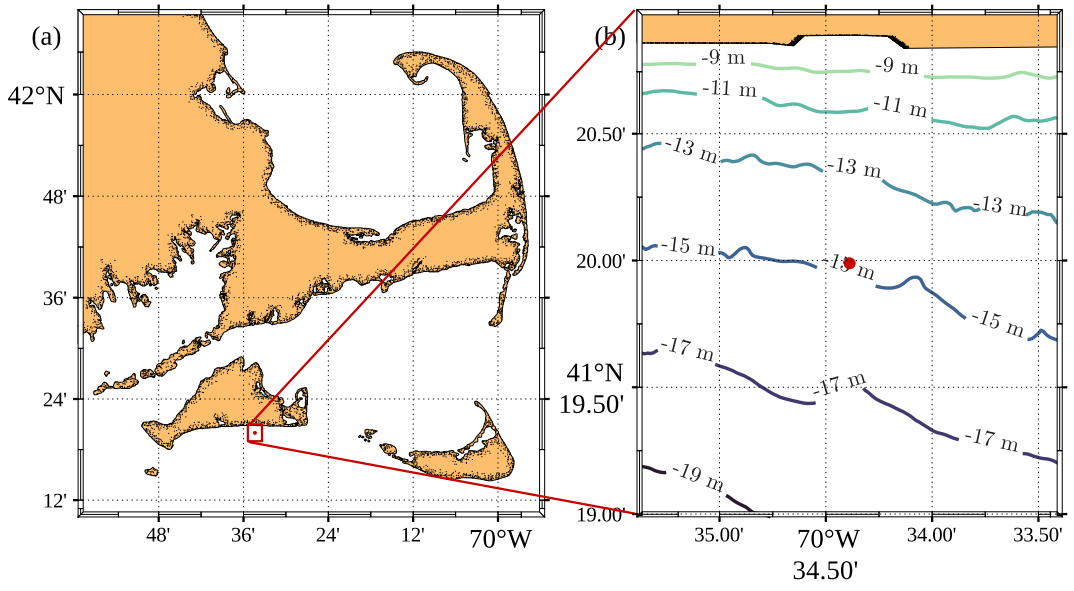

FIG. 2. (a) Map of Cape Cod, Martha's Vineyard, and Nantucket; region of interest marked with red box is shown in (b), with location of ASIT indicated by red circle in the panel center. Colored contours mark water depth (Denny et al. 2008); ASIT sits very close to the 15 m isobath.

The measurement capabilities deployed during the 2019-2020 field campaign at ASIT (hereinafter "ASIT2019") are summarized by Cifuentes-Lorenzen et al. (2024) and Hogan et al. (2025). Here we provide additional information about the sensors and measurements most relevant to the present study. Fixed instrumentation on the tower's horizontally-extended "diving board" provided a mounting point for wave-sensing lidar systems (three Riegl LD90-3 units) for determining the surface gravity wave spectrum and computing the mean water level. An upward-looking Teledyne RDI Sentinel V ADCP was mounted to the seafloor 1 km from ASIT in 18.3 m of depth; this provided an estimate of the frequency-directional wave spectrum every 30 minutes (Cifuentes-Lorenzen et al. 2024). An array of Gill R3 3D sonic anemometers were mounted to the mast on the end of the "diving board" (4.5 m, 8.0 m, and 14.0 m above the mean water level) and Rohn tower

of ASIT (19.5 m and 22.0 m above the mean water level). The full-rate (20 Hz) wind velocity time series $\mathbf{u} = [u\mathbf{x} + v\mathbf{y} + w\mathbf{z}]$ measured by each of the five anemometers was was de-spiked with a three-sample moving median filter and then separated into 20-minute segments. Each segment was further divided into three 10-minute subdivisions, with the middle subdivision overlapping each adjacent subdivision by 50%. Each such snippet was subjected to an Augmented Dickey-Fuller (ADF) test to assess stationarity of the wind velocity (used in this context by Laxague et al. (2015)); subsections which were determined to be stationary by the ADF test passed quality control and their residual linear trend removed. Each snippet was subjected to a Blackman-Harris window before computation of cross-spectra χ_{uw} (streamwise-vertical) and χ_{vw} (spanwise-vertical); a median of each cross-spectrum was computed for each 20-minute segment. The real components (co-spectra C_{uw}, C_{vw}) were then integrated over all frequency to yield the individual directional covariances, from which was produced the wind stress vector $\tau = -\rho_a \left[\langle u'w' \rangle \mathbf{x} + \langle v'w' \rangle \mathbf{y} \right]$ (with ρ_a the air density). The bin-averaged wind speed and stress magnitude profiles (binned by wind speed) are provided in Figure A1. Although the assumption of a constant flux layer may be shaky on a measurement-by-measurement basis (Ortiz-Suslow et al. 2021), the mean behavior in wind speed and wind stress for $z < 15$ m is sufficiently well-behaved to justify our comfort with the assumption. For the analysis which follows, all reported wind stress values were computed from the average over the lowest three (mast-mounted) sonic anemometers [$z = 4.5$ m, 8.0 m, and 14.0 m above the mean water level]. A set of four different cameras was mounted to the Rohn tower on ASIT. Two monochromatic video cameras (Imperx Lynx) with wide angle lenses captured visible imagery of large swaths of the sea surface (approximately 2,580 m^2) to observe whitecaps; the setup of those cameras (as well as the interpretation of the data they collected) is described in detail by Hogan et al. (2025). An adjacent FLIR A6500sc LWIR microbolometer observed the sea surface brightness temperature at 30 frames per second over a $\approx$350 m^2 patch of the ocean, from which the speed and magnitude of the (very) near-surface current was obtained (Liu et al. 2025). The fourth camera—a Polaris Pyxis Mono VIS with the Sony IMX250MZR "Polarsens" detector—is described at length in Laxague et al. (2025a). In short, it provides a measurement of the spatiotemporal variation in polarization state of light reflected from the air-water interface. From this measurement, we employ polarimetric slope sensing (PSS; Zappa et al. (2008)) to infer the ocean surface wave slope field at spatial scales ranging from 3 m – 5 mm and temporal scales down to 1/15 s.

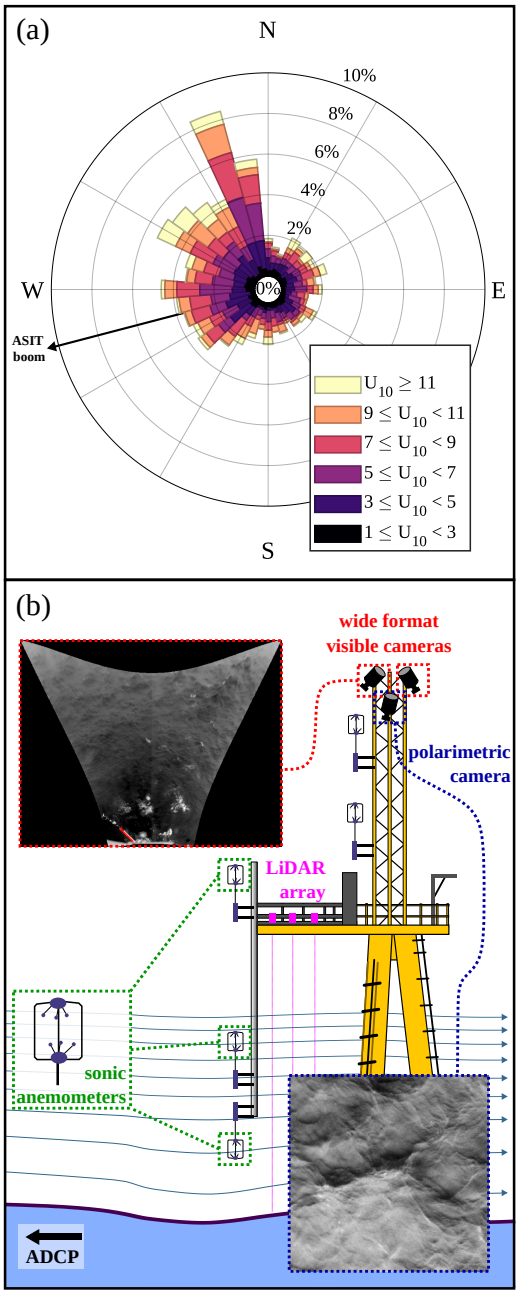

188 FIG. 3. (a) Wind direction-magnitude histogram ("wind rose"), with wind direction provided in meteorological
189 (coming-from) convention. Orientation of ASIT boom (255° true) is indicated by black arrow. (b) Depiction of
190 ASIT and some of the sensors attached during the intensive observational period; inset images depict example
191 frame used for whitecap detection and tracking and a sea surface slope field.

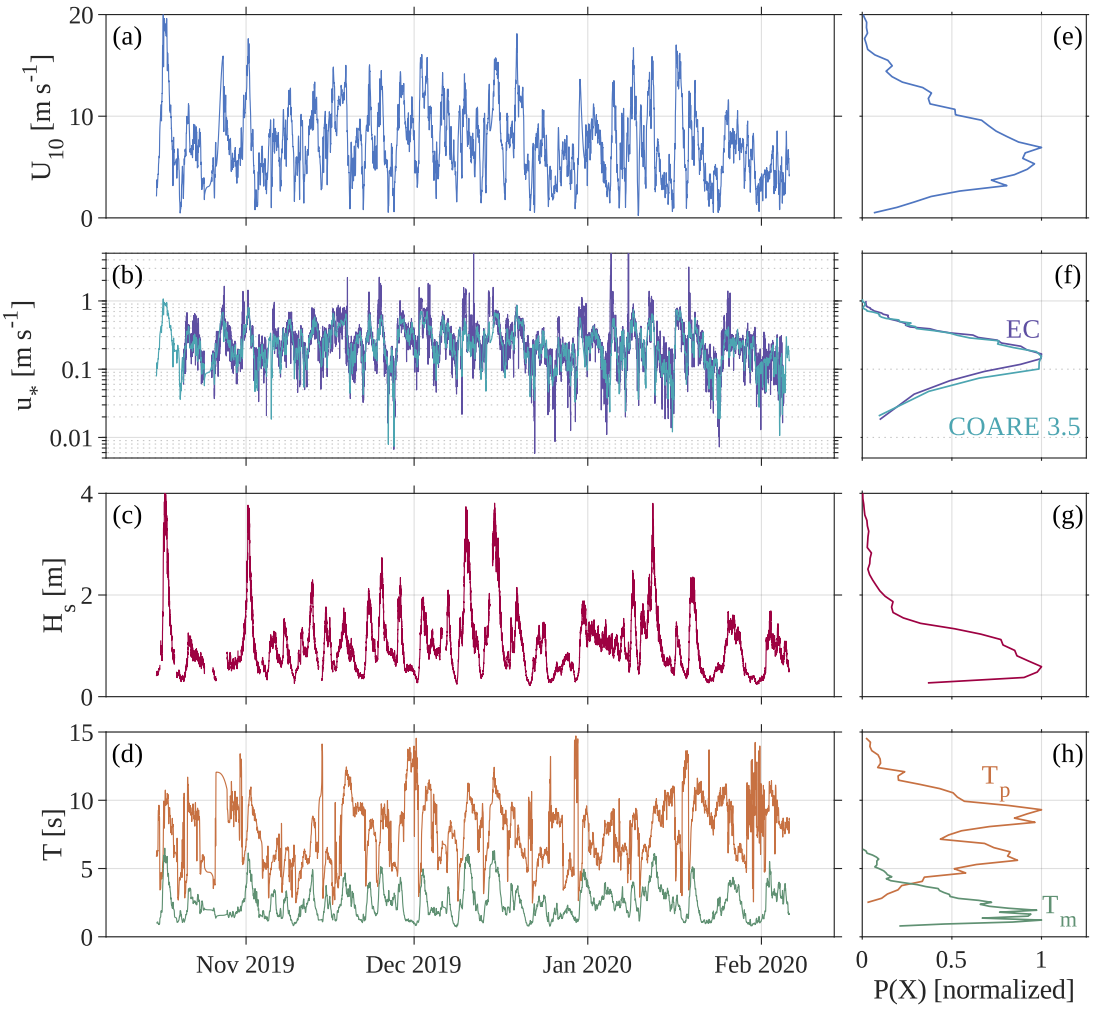

FIG. 4. Time series: (a) ten-meter wind speed (U_{10}), (b) air-side friction velocity u_*, (c) significant wave height H_s, (d) and wave period, both peak (T_p) and mean (T_m). Panels (e)-(h) in the right column provide the corresponding normalized probability density functions.

This study site (and our narrow period of operation) presents a particular challenge for process investigations: wind and waves are often misaligned due to long wave refraction and synoptic-scale weather patterns. To be specific, the dominant wave direction is onshore (i.e., waves propagating northward), though the prevailing wind direction may vary substantially with season or time of day. Indeed, during our observational period, the prevailing wind direction was WSW-NNW (Figure 3a). However, this complication provides an opportunity to examine the variation of off-wind wave propagation over a wide range of angular separations and spatial scales.

A selection of stacked time series of selected observed environmental conditions (with corresponding histograms) is provided in Figure 4. Our measurement period encompassed a wide range of wind speeds (from calm to ≈15 m s^{-1} ten-meter wind speed U_{10}). Significant wave heights varied between ≈0.5 m to ≈3 m, with dominant periods ranging from 4-13 seconds and average wave periods ranging from 1-5 seconds. However, for the investigation that follows, we have used the energy-weighted mean celerity c_E in place of the peak celerity c_p. Energy-weighted mean quantities are generally considered to be analogous to peak quantities (see Figure C1), allowing one to make reasonable comparisons to previous results which are reported in terms of peak quantities. However, energy-weighted mean quantities benefit by being integral moments of the spectra, making f_E (and therefore c_E) robust to changes in frequency-space discretization or elevated bin-to-bin variation. Furthermore, this quantity natively accounts for spectral bandwidth (i.e., the broadness of the peak), which has been demonstrated to be a contributing factor to the air-sea momentum flux (Zhao and Li 2024).

3. Wave Spectral Analysis

The centerpiece of the present study is the short wave observational dataset. Given orthorectified and calibrated measurements of the wave slope over a 3 m × 3 m field of view, repeated at the camera frame rate of 30 fps (Laxague et al. 2025a, e.g.), we may obtain the wavenumber-frequency directional slope spectrum. This process has been described at length elsewhere (Laxague et al. 2015, 2017a, e.g.); we provide a condensed form of the procedure here in appendix 7. The outputs and products of PSS are numerous and diverse: for example, determination of the spectrum of high frequency and high wavenumber wind waves (Laxague et al. 2015, 2018a), inference of the near-surface current profile (Laxague et al. 2017b, 2018b; Laxague and Zappa 2020b), and the effect of rain (Laxague and Zappa 2020a) and biogenic chemical surfactants (Laxague et al. 2024) to suppress short wind waves. Crucially, this technique yields the wavenumber-frequency directional spectrum; this reduces reliance on small-amplitude wave theory, provides a means for quantifying nonlinearity in the wave field (Leckler et al. 2015; Peureux et al. 2018), and enables novel analyses with respect to spectral wave age (Björkqvist et al. 2019).

This portion of the dataset consists of 307 individual ten-minute measurements of short surface wave spatiotemporal evolution, made uniformly across available daylight hours from October 10th,

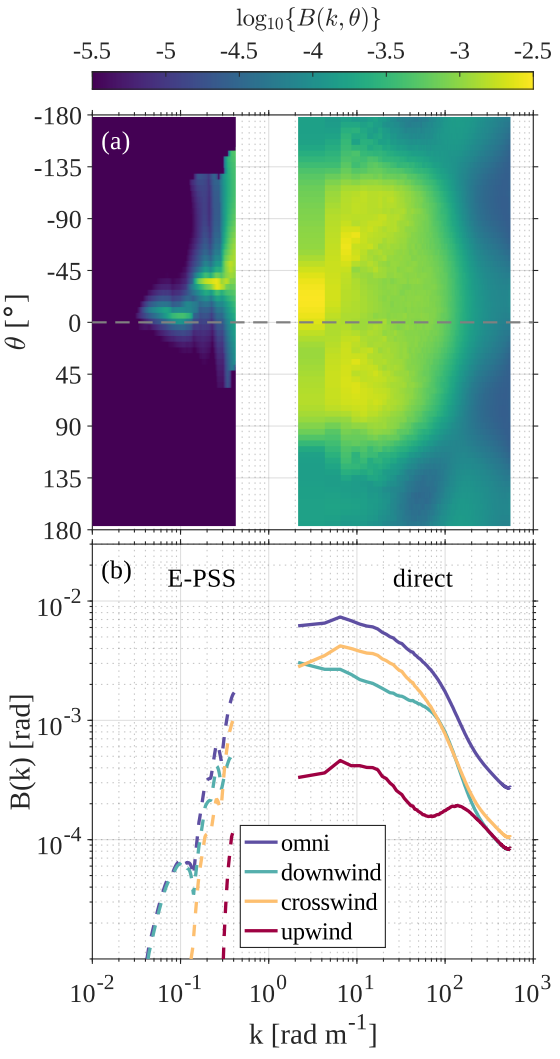

FIG. 5. (a) Example wavenumber-directional saturation spectrum, a composite produced from the E-PSS long wave-derived spectrum (Laxague et al. 2025b) and the direct polarimeter-derived spectrum; angle is given relative to the wind velocity. (b) Direction-integrated spectra (omnidirectional, downwind, crosswind, and upwind).

2019 to February 7th, 2020. Of these, 190 passed initial QC (based on sun glint contamination, low illumination, and motion blur during very strong wind forcing events). The eddy covariance system came online ten days after the first camera acquisition resulting in 143 short wave spectra which had a corresponding eddy covariance wind stress. After excluding cases for which the wind direction approached the anemometers on the ASIT diving board by an angle of greater than 90 degrees, only 56 cases remained. This yield was particularly low due to the offshore prevailing wind direction (Figure 3) during our single season of operation.

In Figure 5(a), we show an example wavenumber directional spectrum obtained from our polarimetric slope field measurements. This spectrum is a composite produced from both direct (i.e., from the Fourier transform of the full slope field stack) and indirect (i.e., through the E-PSS technique of Laxague et al. (2025b)) products of the slope field measurement. The wave direction is given relative to the wind velocity for this case (the horizontal red segment in panel (a)). Panel (b) contains direction-integrated spectra, specifically omnidirectional (violet), downwind (teal), crosswind (goldenrod), and upwind (crimson). This procedure was repeated for each of the 190 camera acquisitions which passed quality control. We note that each technique (direct and E-PSS) suffers in directional fidelity at one extremum in wavenumber. The direct method retrieves energy and direction information from the waves explicitly captured within the spatial field of view (FOV) of the polarimeter. Waves with lengths greater than half the frame size will appear no more than once (and usually, zero times) per frame. This intermittent sampling is likely to have a substantial negative impact on the directional estimate at the lowest wavenumber bin. Consequently, we have established more conservative low wavenumber and frequency cutoffs for the *directional* spectra; graphics subsequent to Figure 5 reflect these cutoffs (k_{low} = 6.47 rad m^{-1}, f_{low} = 1.27 Hz). Conversely, the timeseries-based estimate of the long wave directional spectra (E-PSS) suffers at high frequencies/wavenumbers. These spectra are computed from the sea surface slope timeseries, averaged over the full 3 m × 3 m FOV. This spatial averaging will substantially flatten crests and troughs of waves with lengths near the FOV linear scale; this flattening will attenuate spectral energy density and introduce significant directional ambiguity. We established a high frequency cutoff of f_c = 0.35 Hz, which corresponds to a wavelength λ =12.7 m, or approximately four times the FOV linear scale. Even with this cutoff, a good deal of directional smearing remains near k = 0.4 rad m^{-1} in Figure 5b. Despite these limitations, E-PSS provides the same resolvable frequency range as the directional spectra obtained via our bottom-mounted ADCP. Furthermore, the combination of the direct and extended PSS techniques provides fully-directional spectra over three decades of frequency and five decades of wavenumber, with minimal discontinuity between the two spectra.

Laxague et al. (2025b) demonstrated that the "direct" and E-PSS wavenumber and frequency spectra are consistent in both energy level and slope over the intermediate scales at which the spectra abut one another. In Figure 6, we show the omnidirectional frequency and wavenumber spectra

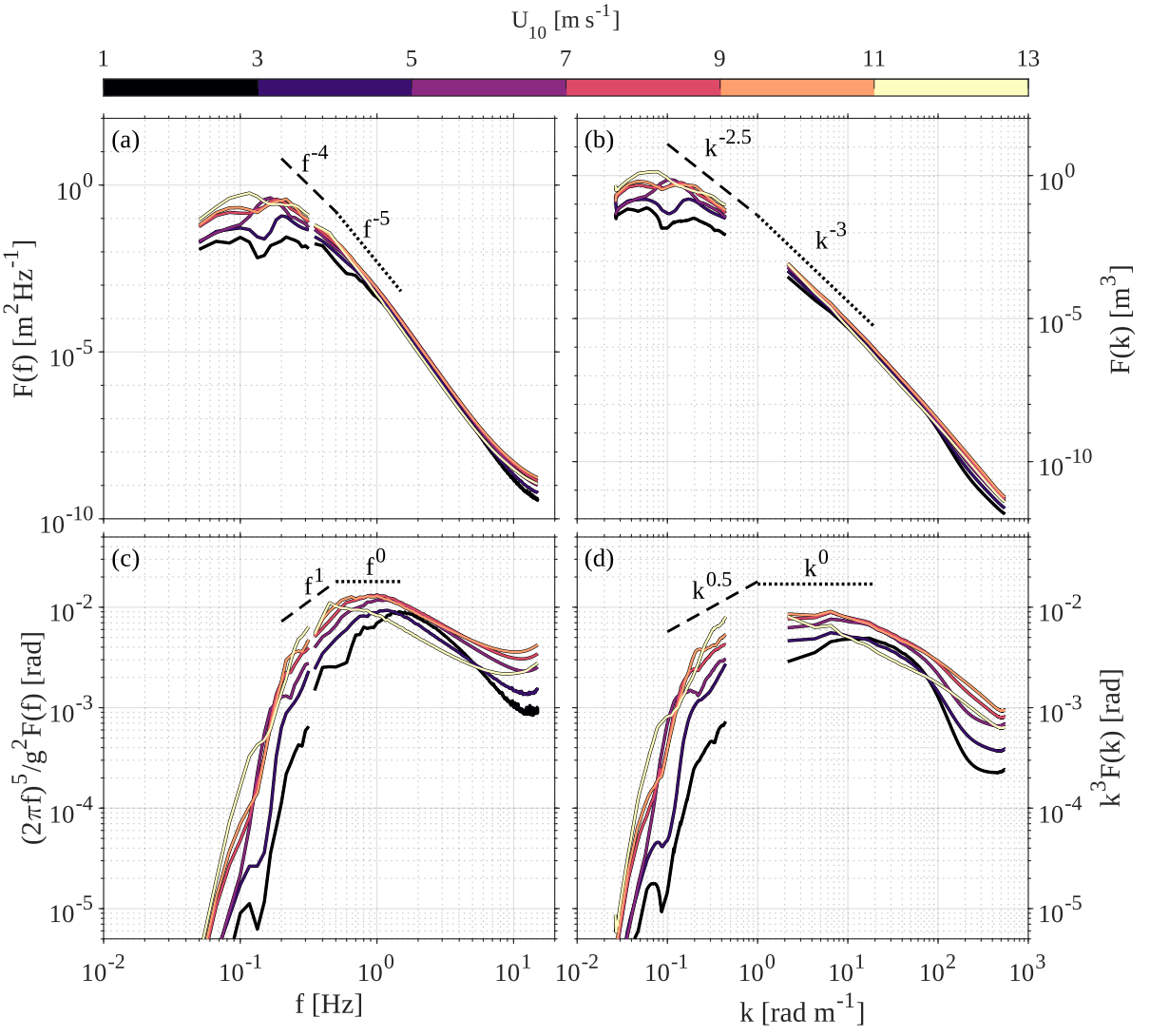

FIG. 6. Frequency and wavenumber omnidirectional spectra for all cases, binned by 10-meter wind speed U_{10}. Panels (a) and (b) show water surface elevation spectra, while panels (c) and (d) show corresponding saturation spectra. Dashed and dotted segments correspond to canonical spectral shapes within the equilibrium and saturation subranges, respectively.

bin-averaged according to the ten-meter wind speed. Panels (a) and (b) provide the elevation spectra while panels (c) and (d) provide the saturation spectra. The right portion of all panels contains spectra produced from the full wavenumber-frequency directional spectra, integrated with respect to direction and either wavenumber or frequency to yield the appropriate omnidirectional spectrum. The left portion of all panels contains spectra computed from the wave slope timeseries

via E-PSS (Laxague et al. 2025b). Those spectra are natively given in terms of frequency, so depth-aware linear dispersion was invoked in order to obtain the long wave wavenumber spectra.

The quantitative measures of wave energy and steepness one may obtain by integrating wave spectra have immense practical value. However, there is likely no application of omnidirectional wave spectra more revealing of the character of the sea state than the interpretation of spectral subrange shape. The canonical equilibrium and saturation range slopes are provided on Figure 6 as dashed and dotted lines, respectively; these subranges are defined in appendix 7. Furthermore, the energy level within the saturation range of the wavenumber spectra (the "degree of saturation", here $5{\times}10^{-3}$-$9{\times}10^{-3}$) is reasonably close to previous observations of this energy level (Banner et al. 1989; Lenain and Melville 2017). Crucially, we note that this saturation range does not persist interminably: at some point between 8-10 rad m^{-1}, we observe a transition to new subrange. The scales at which these subrange transitions occur and the dependence of these transitions on wind forcing represent a shift in the dominant physical mechanisms which control wind-wave development (Phillips 1985). We provide a brief description of our approach for systematically identifying transitions between spectral subranges within appendix 7. This subrange identification is summarized in Figure 7, with subplots providing the variation of frequency and wavenumber-space extrema with ten-meter wind speed. Panels (a-b) contain the absolute magnitude of each estimate, while panels (c-d) contain the estimates normalized by the peak frequency f_p and wavenumber k_p, respectively. The estimate for each individual run is given as a translucent circle, with solid squares corresponding to bin-averaged estimates; the curves of best fit and confidence intervals correspond to least-squares linear regressions performed on the base-ten logarithm of each full dataset.

Generalization of results in this domain requires scaling of appropriate quantities. Phillips (1985) proposed that the upper limit of the equilibrium range k_n should be proportional to g/u_*^2. In Figure 8a, we show wavenumber saturation spectra in terms of nondimensional wavenumber ku_*^2/g, bin-averaged by wind forcing. The forcing chosen is $u_*/\sqrt{gH_s}$, the friction velocity scaled by the "ballistic velocity"– the impact speed of a particle free-falling from height $H_s/2$. As described by Lenain and Melville (2017), this scaling lends itself to wave breaking processes and is more readily defined than the wave age would be in mixed sea or swell conditions. We see that for large values of $u_*/\sqrt{gH_s}$, spectra tend to collapse for higher values of scaled wavenumber ku_*^2/g which

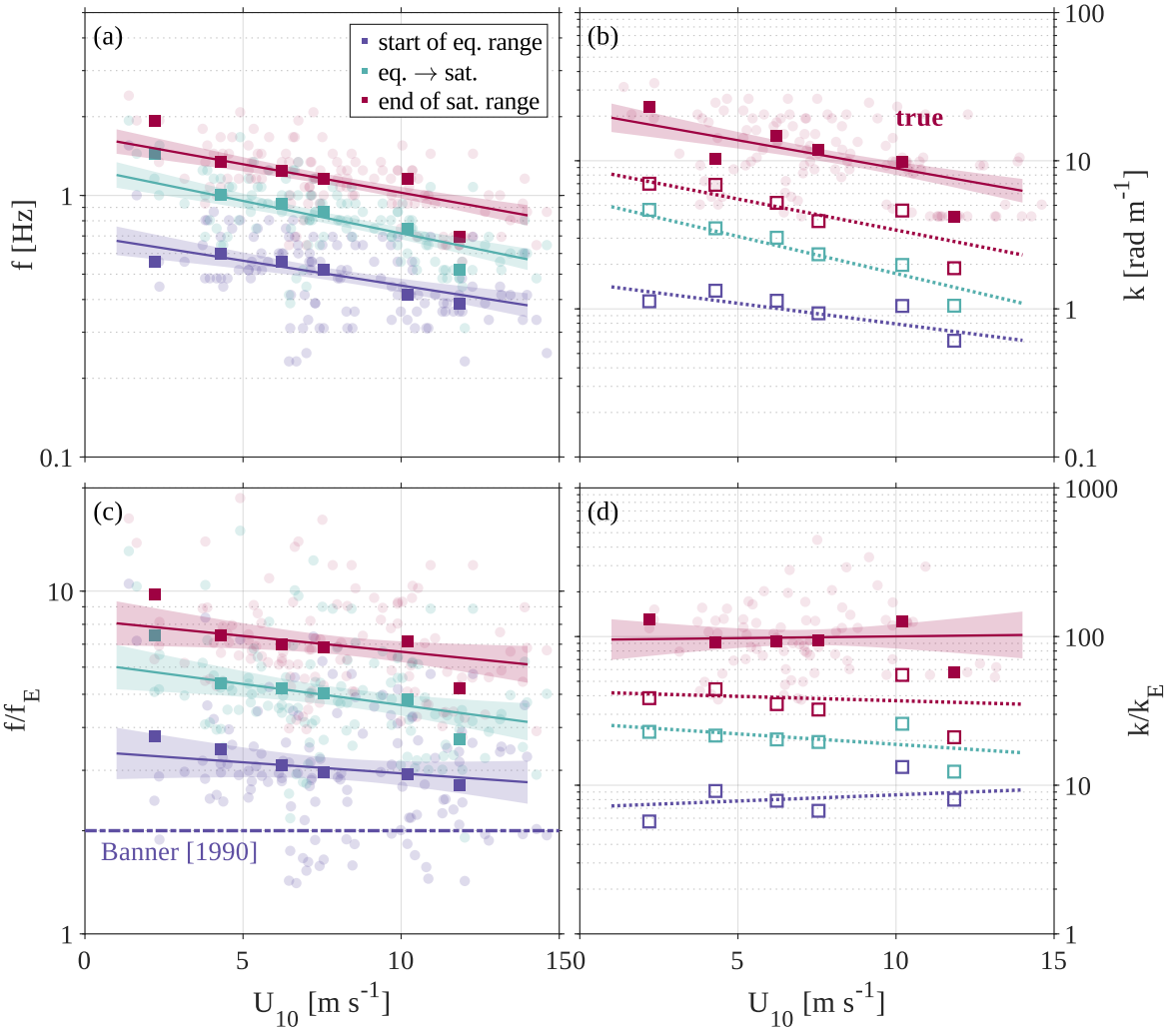

FIG. 7. The frequencies (a) and wavenumbers (b) which mark the lower and upper limits of the equilibrium ($\propto f^{-4}$, $\propto k^{-2.5}$) and saturation ($\propto f^{-5}$, $\propto k^{-3}$) ranges of the water surface elevation spectrum. Panels (c-d) provide the subrange limits normalized by the energy-weighted mean frequency and wavenumber, respectively. The dash-dotted line in panel (c) corresponds to the lower limit of the equilibrium range suggested by Fisher et al. (2017) following Banner (1990). Faint circles mark all data points under consideration, while lines mark least-squares linear regressions to those points with respect to the base-ten logarithm of the independent variable f or k; dashed traces mark 95% confidence intervals about the regressions. Filled squares indicate averages over the wind speed ranges 1-13 m s^{-1} in increments of 2 m s^{-1}. Note that the least-square regressions were computed over all data points (not just those bin-averaged with respect to wind speed).

correspond to saturation and short gravity waves; variations with $u_*/\sqrt{gH_s}$ are seen to occur for the highest wavenumbers (gravity-capillary scale waves). In Figure 8b, we show the variation of k_n with this scaled friction velocity. Our range of observed k_n is consistent with that found by Lenain and Melville (2017), though their response of k_n to $u_*/\sqrt{gH_s}$ is far steeper than ours. There's no single scaling that can account for all variations in wind-wave interaction, so it is possible that the substantially different wave ages (c_E/u_*), depth regimes, and wind-wave alignment conditions between the two datasets has contributed to this disparity. Whether the relationship between k_n and $u_*/\sqrt{gH_s}$ we observe is best described by one side of a shallow parabola (to borrow the functional form suggested by Lenain and Melville (2017)) or some sort of exponential decay (e.g.) is unclear. Resolving this question is left for a future analysis with a larger sample size and a broader range of conditions in $u_*/\sqrt{gH_s}$.

We present the variation of k_n with wave age in Figure 9a alongside results from the airborne observations of Romero and Melville (2010). The teal shaded region and solid line correspond to the 95% confidence interval about the least-squares regression following a modified parametric expression of Hwang and Wang (2001) given the observational data of Romero and Melville (2010). This parametric expression allows one to compute an estimate of the equilibrium-transition wavenumber k_n given wind forcing (u_*) and the energy levels in the equilibrium (β) and saturation (B) spectral subranges:

$$k_n = \left(\frac{2B}{\beta}\right)^2 \frac{g}{u_*^2} \tag{1}$$

Although our measurements were made over slightly older seas than those sampled by Romero and Melville (2010), there is good agreement in the intermediate wave age regime (c_E/u_* ranging from 15-30). This agreement is also shared with the least-squares regression to the observational data of Romero and Melville (2010) given the parametric expression for k_n provided by Hwang and Wang (2001). When this expression is used with our own values of wind forcing and spectral subrange energy levels (Figure 9b), the resulting values of k_n are in good agreement with our observations of k_n ($R^2 = 0.68$, $rmse$ =1.21 rad m^{-1}). The weakest agreement comes for the lowest values of k_n/k_E modeled by equation 1. This may be a shortcoming of the model, though it is quite possibly due to a limitation in our technique for spectral subrange identification; our wide frequency-space regression windows offer robustness with respect to sharp variations in the

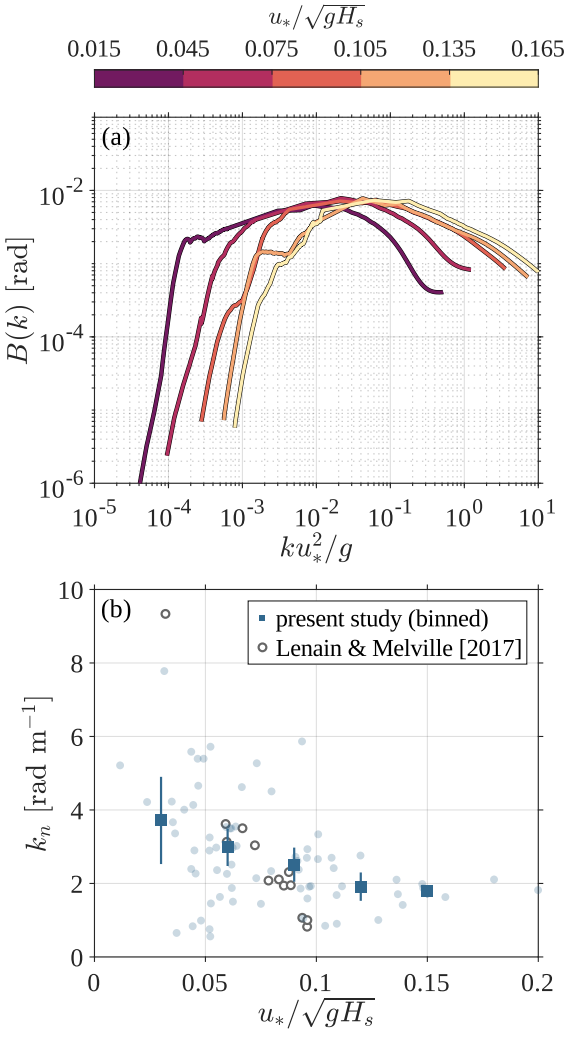

330 FIG. 8. Variation of (a) omnidirectional wavenumber saturation spectra and (b) equilibrium-saturation transition
331 wavenumber with wind forcing; partially-transparent circles indicate all observations, while filled squares (and
332 vertical errorbars) correspond to bin averages (and 95% confidence intervals). Wavenumber in (a) and wind
333 forcing in (b) have been scaled following Lenain and Melville (2017).

351 frequency spectrum, but this coarseness reduces our resolution near the spectral peak. Therefore,
352 we would be expected to overestimate k_n in the event that it was particularly close to k_E.

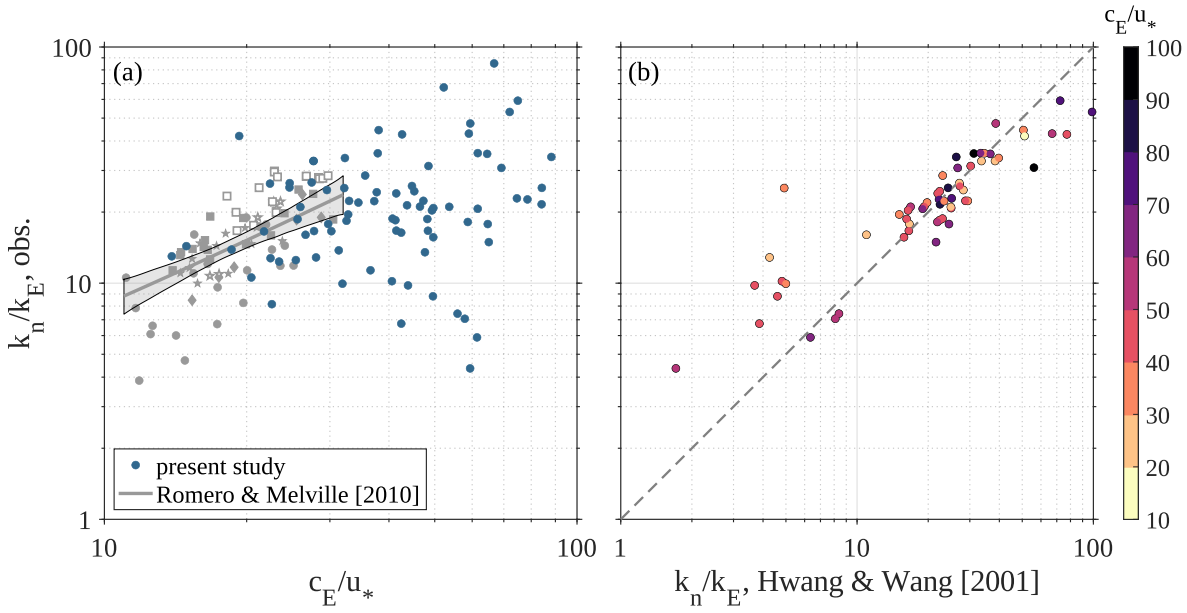

FIG. 9. (a) Variation of equilibrium-saturation transition wavenumber k_n normalized by energy-weighted mean wavenumber k_E. Violet circles mark our measurements, while teal markers indicate those made by Romero and Melville (2010); marker style corresponds to their segmentation by research flight. The line and shaded region mark a least-squares regression computed from the observational data of Romero and Melville (2010) when passed through a parametric model for k_n by Hwang and Wang (2001). (b) Scatterplot of our observations against the same model, with the dashed line marking 1:1 agreement.

Further insight into the nature of these transitions in omnidirectional spectral shape and the physical mechanisms which drive them will come from investigation of the directional characteristics (e.g., mean direction and spreading/modality) of the wavenumber-directional and frequency-directional spectra. For the purposes of convenient comparison between wavenumber and frequency-directional spectra, we define a generic form of a scaled directional spectrum:

$$B^*(X,\theta) \equiv \frac{B(X,\theta) - \min\{B(X,\theta)\}}{\max\{B(X,\theta)\} - \min\{B(X,\theta)\}} \tag{2}$$

... where X is an independent variable in Fourier space (e.g., k or f).

A directional spreading function $D(X,\theta)$ may be defined in a variety of ways, depending on the requirements of the application. We are interested in obtaining the angular extent to which the spectral energy density decreases from its maximum value (not necessarily its downwind value), so we define D as follows:

$$D(X,\theta) \equiv \frac{B^*(X,\theta)}{\max_X\{B^*(X,\theta)\}} \tag{3}$$

... where $\max_X\{B^*\}$ represents the maximum value of B^* at each value of X.

This function does not behave as the typical directional spreading function that, when multiplied by the omnidirectional spectrum, yields the fully-directional spectrum. However, the normalization to unity at each wavenumber/frequency allows us to visualize the relative spreading without considering scale-dependence of the spectral energy density. To wit: examples of B^* and D computed from the same 10-minute acquisition are provided in Figure 10.

There is no single measure to be used for describing directional spreading and modality. Past studies which have investigated bimodality within the equilibrium range of the wave spectrum (Romero and Melville 2010; Lenain and Melville 2017, e.g.) defined lobe separation angle and the ratio between downwind and lobe spectral energy density. As our field of view is confined to $\approx$3 m $\times$ 3 m, we cannot adequately describe the transition from a unimodal sea to a bimodal sea in the equilibrium range. As such, we do not attempt to define the aforementioned lobe parameters. In place of these metrics we compute two quantities to characterize directional spreading and spectral bimodality. The first of these is the 50^{th} percentile contour in the directional spreading function $D(X,\theta)$. We use this metric in place of other quantifications of spreading (e.g., σ_θ, Lin

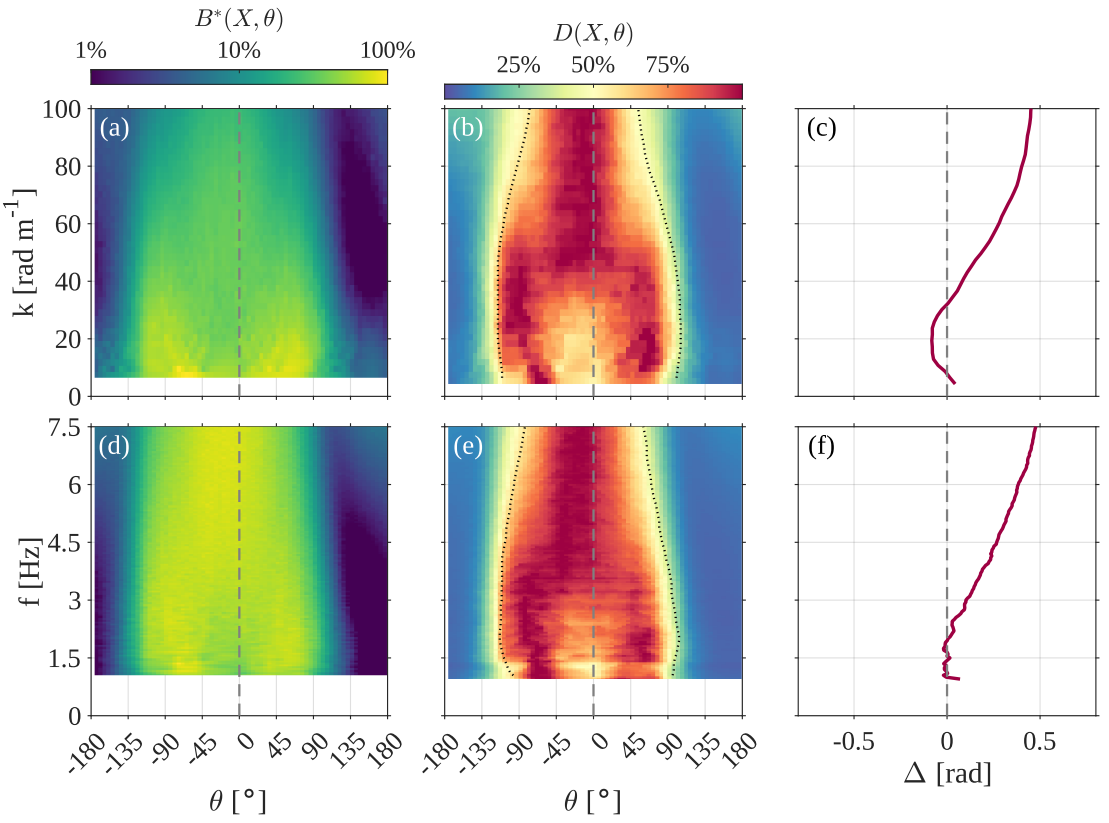

FIG. 10. Example wind-relative directional spectra (given in terms of (a) wavenumber and (c) frequency), taken from observation for which U_{10} = 10.25 m s^{-1} and c_E/u_* = 27.8. Left column: directional saturation spectra. Spectral energy densities are normalized according to equation 2. Middle column: directional spreading function D, defined according to equation 3; the 50$^{\text{th}}$ percentile of $D(X,\theta)$ is overlaid as a black dotted contour. Right column: corresponding directional spreading ratio Δ as defined by equation 4.

et al. (2022)) because it provides a straightforward and readily interpretable measure of the wave directional spreading envelope.

The second quantity we compute to assess spreading (and where applicable, detect bimodality) is the directional spreading ratio Δ from Elfouhaily et al. (1997). We have modified it to compute the average of the spectrum at $\theta = \pm 90°$ (rather than their original evaluation at +90°), and to allow the $\theta = 0°$ centerpoint to be the wavenumber-dependent mean wave direction. These tweaks were intended to allow for better characterization of sea states with asymmetric directional spreading and with strong directional veering.

$$\Delta(X) \equiv \frac{B^*(X,0) - \overline{B^*(X,\pm 90^\circ)}}{B^*(X,0) + \overline{B^*(X,\pm 90^\circ)}} \tag{4}$$

Note that a large value of Δ indicates relatively high spectral energy density in the mean down-wave direction. A Δ value of zero represents no difference between in spectral energy density between down-wave and cross-wave directions. A negative value of Δ indicates that the spectral energy density is greater in the cross-wave direction than the down-wave direction (i.e., the presence of bimodality).

4. Wave Breaking Analysis

Wave breaking is a crucial element of the wind-wave balance (Banner and Melville 1976; Phillips 1985), helping to determine the canonical shape of the wave spectrum and shaping its directionality (Romero and Lubana 2022). In this section, we describe our application of the Duncan-Phillips framework for quantifying the energy and momentum flux associated with surface wave breaking, though we won't attempt to explain any concepts more thoroughly than has been done before (the reader can turn to Romero (2019) for greater detail). Duncan (1981, 1983) demonstrated that the energy dissipated per unit crest length by a single breaker may be given by:

$$\epsilon_l = \frac{b\rho_w c^5}{g} \tag{5}$$

... where b is a non-dimensional "breaking strength", c is the breaker speed, ρ_w is the density of water, and g is the acceleration due to gravity. Phillips (1985) extended this concept to multi-component wave fields with arbitrarily many breakers of different speeds and directions. To be specific, if one is able to identify and track breaking wave crests on the ocean surface, one may compute a distribution of those breaking crest lengths in terms of their speed and direction. This distribution is named the breaking crest length distribution $\Lambda(c,\theta)$. As is the case with analogous statistical distributions, its value lies in the specific physical interpretation of its integral moments. We highlight two of these moments. The first of these follows directly from Duncan's result for energy dissipation ϵ_l:

$$\mathcal{F} = \frac{\rho_w}{g} \iint b c^5 \Lambda(c,\theta) c \mathrm{d}c \mathrm{d}\theta \tag{6}$$

here, $\mathcal{F}$ is the total energy dissipated by surface wave breaking per unit area per unit time (i.e., the surface energy flux in W m^{-2}). Similarly, the momentum flux (in N m^{-2}) imparted to the ocean via wave breaking is given by:

$$\tau_{\mathbf{br}} = \frac{\rho_w}{g} \iint b c^4 \Lambda(c,\theta) \mathbf{c} \mathrm{d}c \mathrm{d}\theta \tag{7}$$

In practice, the breaking strength b varies by orders of magnitude depending on the blend of environmental conditions at play. It has been shown to depend strongly on the slope of the incipient breaker (Drazen et al. 2008), though in complex field conditions this is most readily approximated through parameterization of b in terms of the spectral energy density in the saturation range (Romero et al. 2012; Romero 2019). However, we employ the wave age-based approach of Zappa et al. (2016):

$$b = A + B\frac{c_p}{u_*} \tag{8}$$

... where A and B are empirical parameters. Zappa et al. (2016) determined them to be A = 3.482×10^{-3} and B = -4.691×10^{-5}; we use the values (A = 2.027×10^{-3}, B = -2.166×10^{-5}) which Hogan et al. (2025) obtained by fitting the wave age-based formulation of b (equation 8) to the values of b determined by Romero et al. (2012). We chose to define an effective b for all scales of breaking in a given wave state in order to retain Duncan's original scaling of $\epsilon_l \sim c^5$ (and therefore Phillips' $\epsilon \sim c^5\Lambda(c)$), rather than introducing a scale dependence to b.

In the context of numerical wave modeling, it is convenient to stop short of integration over all scales and direction, instead quantifying the energy dissipated by particular wave components. The energy dissipated by waves on $[c, c+\mathrm{d}c], [\theta, \theta+\mathrm{d}\theta]$ is given by:

$$S_{ds}(c,\theta) c \mathrm{d}c \mathrm{d}\theta = \frac{b}{g^2} \Lambda(c,\theta) c^5 c \mathrm{d}c \mathrm{d}\theta \tag{9}$$

However, wave spectra are generally presented in terms of wavenumber k (or frequency f). We employ deep-water small-amplitude wave theory to infer k given c. The wave dissipation source function S_{ds} may be represented in terms of wavenumber k in the following manner: $S_{ds}(k,\theta) = -\frac{\partial c}{\partial k}\frac{c}{k} S_{ds}(c,\theta)$. An example breaking crest length distribution $\Lambda(c,\theta)$ and its corresponding wavenumber-dependent dissipation source function $S_{ds}(k,\theta)$ is provided in Figure 11. The visible

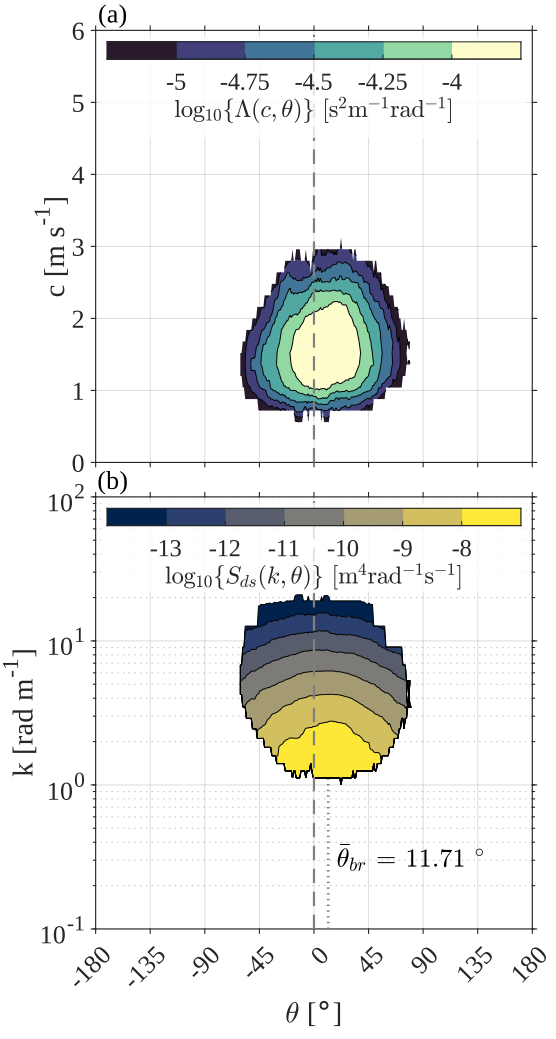

448 FIG. 11. (a) Breaking crest length distribution $\Lambda(c,\theta)$ for a particular observational case. (b) Corresponding
449 wave dissipation source function $S_{ds}(k,\theta)$ produced following eq. 9. Direction is given in degrees relative to
450 the wind (demarcated by the gray dashed lines).

442 white caps which contribute to our $\Lambda(c,\theta)$ are associated with waves with celerities between ≈0.8
443 m s^{-1} and 3 m s^{-1}. Invoking small-amplitude wave theory, we determine that this corresponds
444 to wavenumbers between ≈1-20 rad m^{-1}. The mean breaker direction $\bar{\theta}_{br}$ is not necessarily
445 aligned with the wind direction, though that quantity is heavily weighted towards the longer, more
446 energetic breakers. The slowest breaking fronts (corresponding to the shortest waves) do appear to
447 be predominantly spread about the wind direction.

The colored contours on the wavenumber-directional spectrum within Figure 12a represent the dissipation source function $k^4 S_{ds}(k,\theta)$, compensated to match the saturation spectrum $B(k,\theta) = k^4 F(k,\theta)$. As shown in Figure 11, for this case the mean direction $\bar{\theta}_{br}$ is oriented a bit to the right of the wind direction. However, at higher wavenumbers, the dissipation source function contours are strongest in the downwind direction, matching the qualitative bimodality at $\approx$10 rad m^{-1}. The dark red trace on Figure 12b was produced by integrating S_{ds} over wavenumber (preserving the directional dependence). Similarly, the blue solid trace with dotted bounds corresponds to the scale-integrated wind input source function S_{in}; the difference between the scale-integrated wind input and dissipation source functions is provided in panel (c). We have used a version of S_{in} which follows the wave generation mechanism of Miles (1957), formulated in terms of spectral wave age (Plant 1982; Janssen 1991), with empirical scaling coefficients and uncertainty bounds inferred from classic laboratory and field observations (Plant 1982). Although newer versions of this source function exist (e.g., the Mueller and Veron (2009) framework which accounts for feedback effects associated with airflow sheltering), we chose the simplest version of the function for this example. We note that, although we provide no error quantification for τ_{br}, there is expected to be substantial uncertainty in b (Zappa et al. 2016). We further note that the propagation of any errors in c into any higher-order moments (e.g., τ_{br}) would be substantial.

As shown in Figures 11 & 12, the mean breaker propagation direction may be misaligned with the wind direction. In order to compare wave breaking characteristics across multiple acquisitions, we need to ensure that the dissipation source functions across all runs are directionally aligned. We have accomplished this task by subtracting $\bar{\theta}_{br}$ from our direction independent variable for each case such that all estimates of $S_{ds}(k,\theta)$ have the same mean direction. In Figure 13a, we show the variation of wave breaking momentum flux with direction bin averaged by wave age. We find the energy flux curves to be well-behaved and decreasing in amplitude with increasing wave age up to the bin centered on $c_E/u_* = 40$.

Figure 13b contains the directional momentum flux curves normalized by amplitude. The shaded bars underneath the curves demarcate the interdecile (10^{th}-90^{th} percentile) and interquartile (25^{th}-75^{th} percentile) ranges of variation. We see that the energy flux is distributed more tightly about the mean direction for younger waves than for older waves. As shown in Figure 14a, the breaking angle $\bar{\theta}_{br}$ deviates from the wind direction with increasing wave age up to $c_E/u_* \approx 35$.

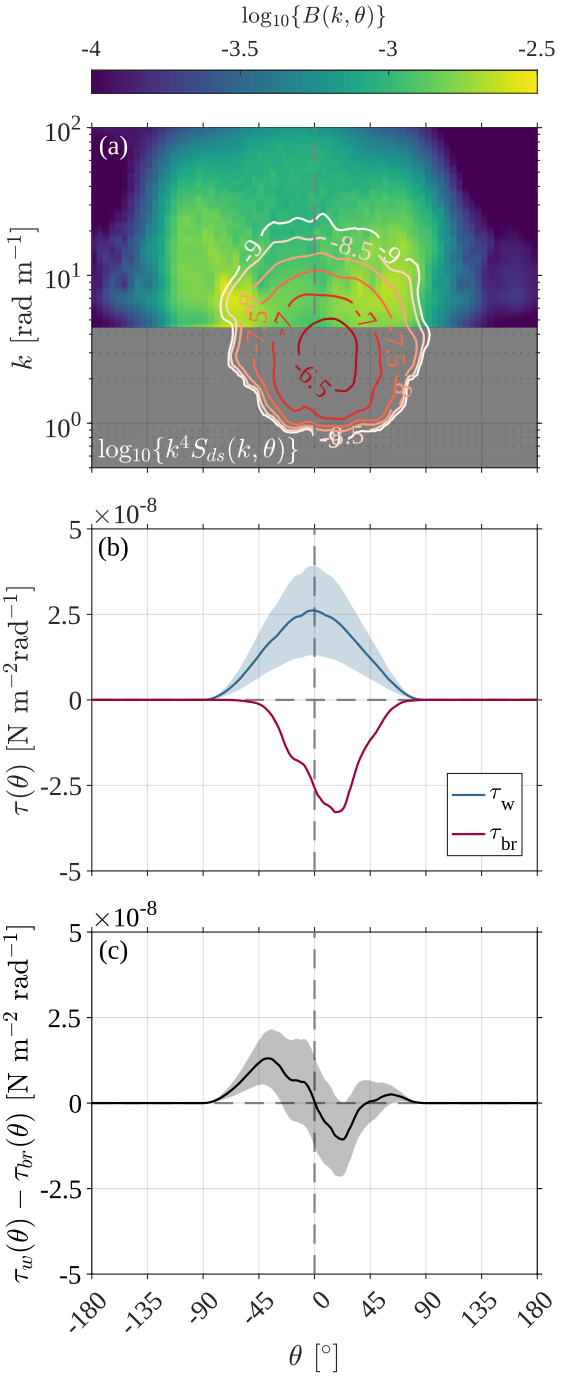

FIG. 12. (a) wavenumber-directional saturation spectrum trimmed at k_{low} = 6.47 rad m^{-1}; overlaid contours correspond to the compensated dissipation source function $k^4 S_{ds}(k,\theta)$, (b) wind input (S_{in}) and dissipation (S_{ds}) source functions integrated up to the upper limit of the saturation range, (c) wind input less dissipation. Direction is given in degrees relative to the wind (demarcated by the gray dashed lines).

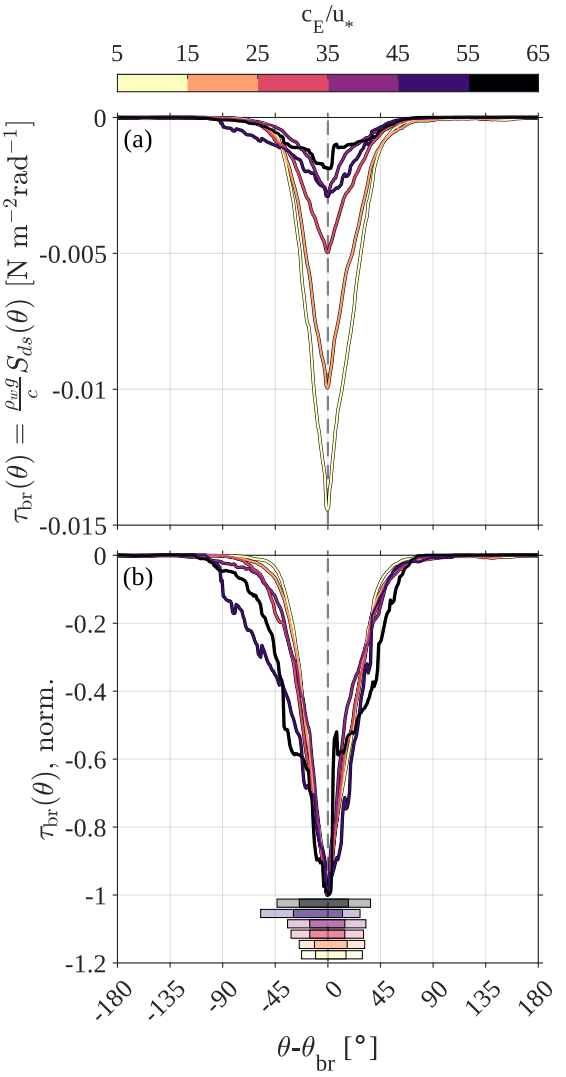

480 FIG. 13. Wavenumber-integrated momentum flux associated with breaking fronts, $\tau_{br}(\theta)$: (a) bin-averaged
481 by wave age, (b) same averaging, normalized by maximum amplitude. Horizontal bars at the base of the panel
482 demarcate the interdecile and interquartile ranges of $\tau_{br}(\theta)$.

488 Furthermore, Figure 14b reveals that total energy dissipated decreases monotonically with wave age
489 until $c_E/u_* \approx 35$. For seas which are "older", it appears that breaker behavior begins to decouple
490 from the wind forcing in both direction and magnitude. This result is in good agreement with the
491 findings of Sutherland and Melville (2013), who employed the same Duncan-Phillips framework
492 to a set of observations made in sea states with an analogous range of wave ages.

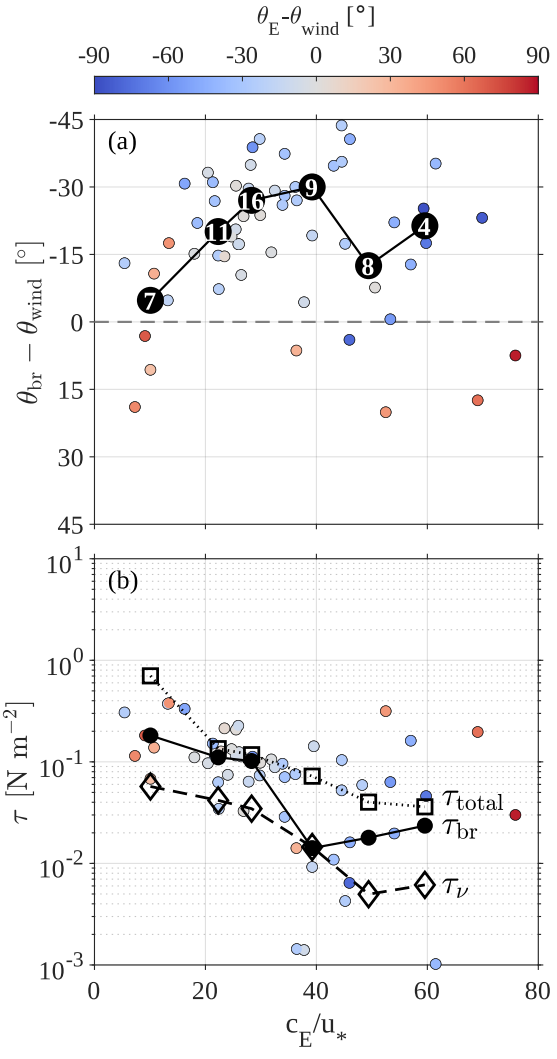

493 FIG. 14. Variation of wave breaking-derived parameters with wave age: (a) off-wind mean breaker angle, (b)
494 momentum flux: total (squares), viscous (diamonds), and wave breaking (circles). Wave breaking momentum
495 flux was computed from the fourth moment of $\Lambda(c)$ via equation 7; colored circles represent the individual
496 measurements, with color indicating the off-wind long wave direction. Filled black symbols correspond to bin
497 median values of the dependent variables with respect to fixed-width wave age bins (following the convention
498 used herein). The white numbers in the black squares of panel (a) mark the number of samples per bin. Water-side
499 viscous stress measurements were taken from Liu et al. (2025).

5. Wave Spectral Directionality

a. Mean Direction

In Figure 15, we present the angular misalignment between the wind velocity and select components of the surface wave and current field. For this particular visualization, we do not distinguish cases by wind speed; our independent variable is simply the difference between energy-weighted mean direction and wind direction. Our intent is to quantify the relationship between wind/short wave alignment and wind/long wave alignment through direct comparison of the two residuals. We decompose the broad category of "short" waves into the aforementioned equilibrium and saturation subranges as well as shorter regimes defined by the Bond number Bo, a nondimensional balance between gravity and capillarity (Hager 2012). This mode of separation has been utilized in laboratory (Veron and Melville 2001) and field (Laxague et al. 2015) studies of very short wind waves. The panels of Figure 15 are divided as follows: (a) equilibrium range (as determined through the methods described earlier in this section), (b) saturation range (as determined through the methods described earlier in this section), (c) short gravity range (waves with Bond number $Bo >$ 10, wavelengths $\lambda >$5.3 cm), (d) gravity-capillary range (waves with Bond number 10$< Bo <=$ 0.1, wavelengths 5.3 cm $> \lambda >$5.3 mm). We also provide a measure of misalignment between wind and (e) the propagation direction of breaking fronts and (f) the direction of the near-surface current. Measurements of breaking wave characteristics (Hogan et al. 2025) and near-surface current (Liu et al. 2025) were made with different imaging systems, each with its own sampling interval and quality-control concerns. Consequently, the individual measurements of wind waves and breakers/near-surface current are not comparable on a 1:1 basis. Individual measurements are provided as filled colored (by wave age) circles, while the lines and shaded regions correspond to least-squares linear regressions computed on $|\theta_E - \theta_{wind}| \leq 90°$ and the corresponding 95% confidence intervals about those regressions. Note that the vertical axis is again flipped relative to its default orientation, so a positive correlation is indicated by a downwardly-sloping line.

The linear regression analysis reveals positive correlations between the short wave / wind difference and long wave / wind difference for the following regimes: equilibrium, saturation, and breakers (table 1). For waves within those subranges, if the dominant wave direction and the wind direction are misaligned by no more than 90°, there is a tendency for the shorter wind-waves to

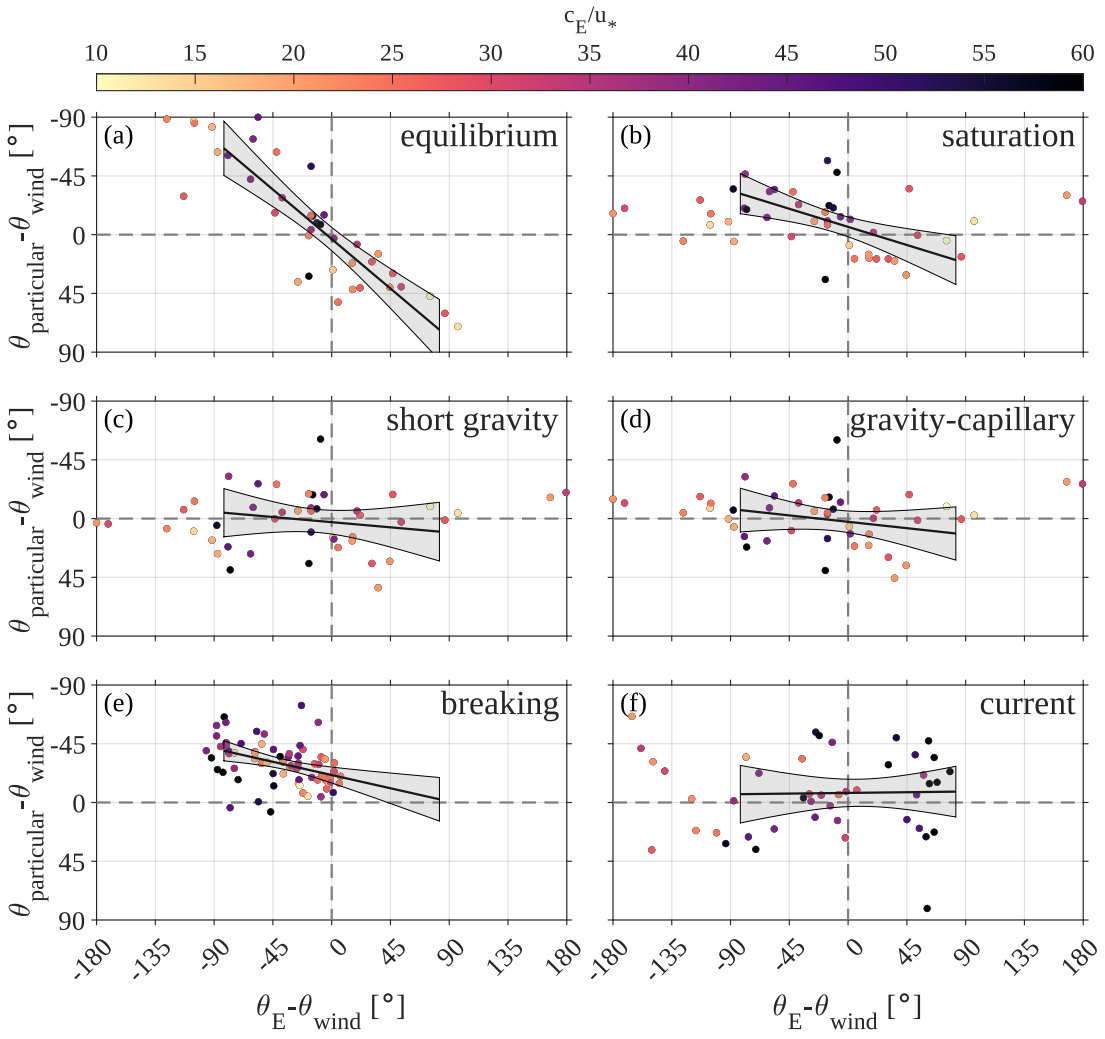

FIG. 15. Variation of short wave/wind relative angle with long wave/wind relative angle. Panels correspond to short waves in the (a) equilibrium range, (b) saturation range, (c) short gravity range, (d) gravity-capillary range; panels (e) and (f) correspond to visible breaking waves (Hogan et al. 2025) and near-surface current (Liu et al. 2025), respectively. Marker color indicates wave age c_E/u_*. Lines correspond to least-squares linear regressions, with shaded regions demarcating the 95% confidence intervals of those regressions.

be misaligned in the same direction, albeit to a lesser extent (regression slopes are less than one). The negative results here also tell a story: misalignment between the dominant wave direction and the wind direction does not reliably "steer" short gravity waves, gravity-capillary waves, or the near-surface current off the wind direction. Liu et al. (2025) found that, despite substantial case-by-case variability in near-surface current direction, there was not a mean (or even reliably

Subrange	Line Slope	Line Slope p-Value	R^2
Equilibrium	0.843	1.068×10^{-7}	0.629
Saturation	0.308	0.002	0.252
Short Gravity	0.088	0.429	-0.012
Gravity-Capillary	0.110	0.283	0.006
Breakers	0.225	0.002	0.129
Current	-0.012	0.913	-0.029

TABLE 1. Results from least-squares linear regression analysis comparing long wave / wind misalignment with short wave (or current) / wind misalignment. Rows with dark red text correspond to subranges with statistically significant regression line slopes ($p < 0.005$).

wind-dependent) offset from the wind direction. We add to this result by finding that neither the misalignment between long waves and wind (or even the off-wind propagation of breaking fronts, which themselves are known to contribute to the near-surface drift) have a measurable impact on the direction of the near-surface current.

b. Directional Spreading

In this section, we present the frequency and wavelength dependence of the two key directional spreading parameters introduced in section 3 ($\theta_{\text{halfwidth}}$ and Δ). In order to extend our analysis beyond the wavenumber at which we lose corresponding temporal information (which resolves the 180° ambiguity), we visually identified the downwind and upwind portions of the wave spectrum for each of the 190 cases, at which point the portions were masked and systematically subjected to the procedure described in section 3. As shown in Figure B1, this ambiguity is usually quite simple to resolve qualitatively by eye. Performing this procedure yielded access to the directional characteristics of the gravity-capillary subrange ($k > 117$ rad m^{-1}). Figure 16, provides the variation of these quantities with respect to nondimensional wavenumber following Phillips (1985): $\hat{k} \equiv ku_*^2/g$; this nondimensionalization was also used as part of the analysis described by Lenain and Melville (2017). In order to more clearly separate results at different wave ages, we have bin-averaged our observed spreading information by that variable; filled circles/squares and horizontal line segments correspond to the upper limits of the equilibrium/saturation ranges

as inferred from the omnidirectional spectra (Figure 7). Although the observations of Lenain and Melville (2017) were made in seas older than the ones sampled in our campaign ($30 < c_E/u_* < 120$ for their measurements), we note that our normalized transition wavenumbers $\hat{k}_n$ show good agreement with their reported values of $r \equiv k_n u_*^2/g$ for similar wave ages (i.e., the vertical positions of the horizontal shaded bars in Figure 16b). Shaded bars which are elongated in the vertical direction correspond to the interdecile ranges in wavenumber and angular width of our observed $\tau_{br}(k,\theta)$, as originally shown in Figure 13b. We see that the surface wave scales associated with breaking wave momentum flux occur near the transition between the equilibrium and saturation spectral subranges. Furthermore, the characteristic width of τ_{br} is narrower than the width of the wave spectrum itself– particularly for the youngest waves $c_E/u_* < 35$. We do not have a great deal of reliable directional information at scales near the equilibrium-saturation transition (notice that $\theta_{halfwidth}$ and Δ have been truncated at low $\hat{k}$). We see that $\theta_{halfwidth}$ monotonically decreases for increasing wave frequency (here converted to wavenumber and then scaled as $\hat{k}_{disp}$ within Figure 16a-b). However, the direct determination of the wavenumber-directional spectrum (with spreading parameters provided in Figure 16c-d) give access to even smaller surface waves.

The key features and defining trends of wave directionality with varying wind forcing are particularly salient when one normalizes the nondimensional wavenumber by the wavenumber(s) of subrange transition. In Figure 17a, we see that the characteristic wave breaking scale straddles the transition between the equilibrium and saturation ranges. We now see the results presented in Figure 16 more cleanly summarized. The monotonic variation of $\theta_{halfwidth}$ and Δ with frequency can be attributed to the fact that the frequency spectra only provide directional characteristics of the saturation and short gravity ranges (i.e., the horizontal shaded bars in Figure 17a demarcate the upper limit of the latter regime). In contrast, the direct wavenumber spectra provide access to directional characteristics of the short gravity and (beginnings of the) *gravity-capillary* subranges. We see that for wavenumbers greater than the upper limit of the saturation range, the spectrum narrows and tends to become more strongly unimodal (Figure 17c,d). For reference, the horizontal shaded bars overlaid on Figure 17d correspond to $k = 371$ rad m^{-1} ($\lambda \approx 1.7$ cm, $c_{min} \approx 23$ cm s^{-1}).

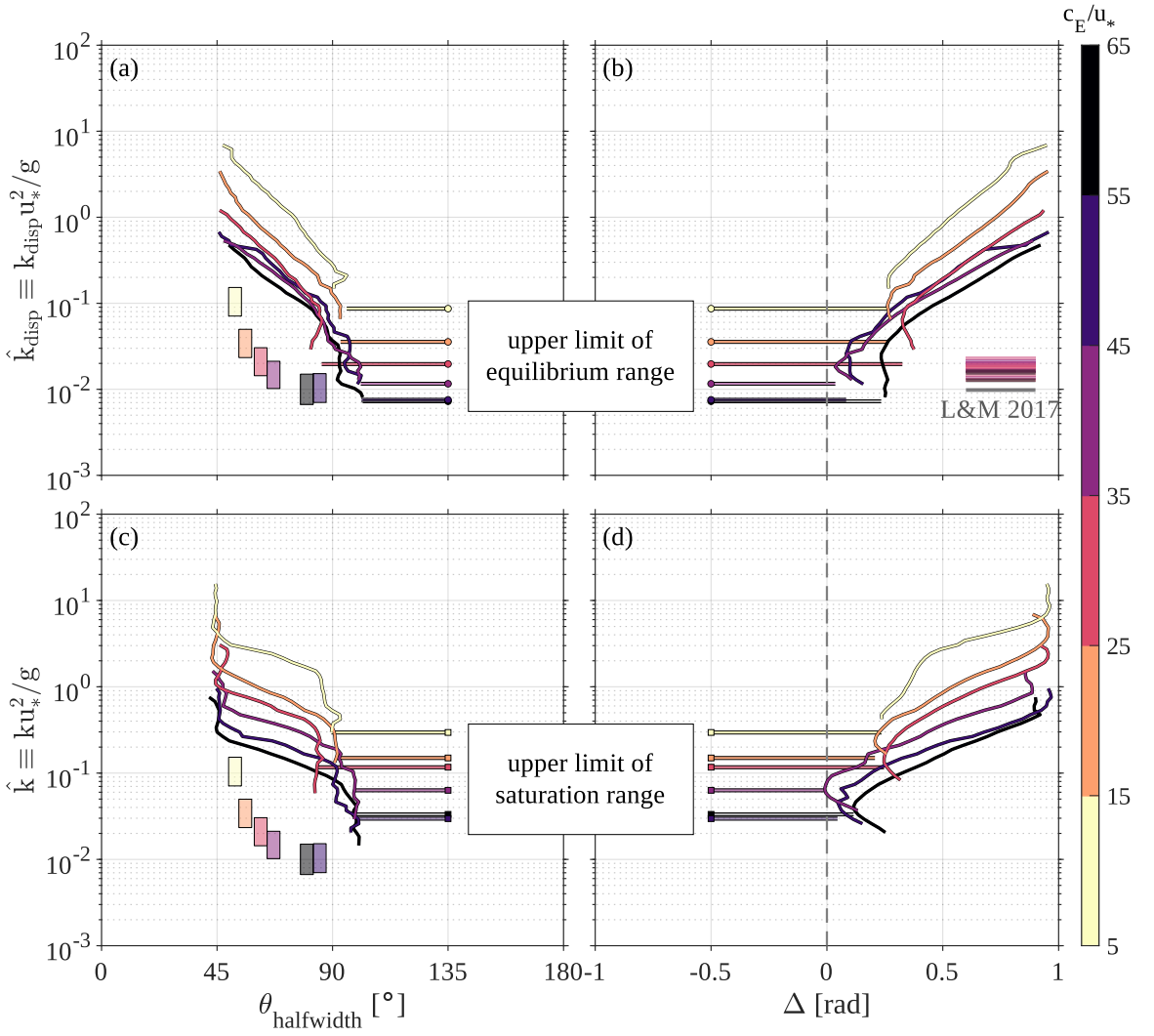

FIG. 16. Frequency and wavenumber-directional spectrum spreading information: panels (a,c) The angle between the mean short wave direction and the 50th percentile in D; panels (b,d): the spectral spreading ratio Δ. The vertical axes represent the non-dimensional wavenumber following Phillips (1985): $\hat{k}_{disp} \equiv \omega^2 u_*^2/g^2$ assuming linear dispersion in deep water (a,b); $\hat{k} \equiv k u_*^2/g$ directly from the wavenumber spectrum. Color indicates wave age c_E/u_*. Filled circles (with corresponding horizontal colored bars) demarcate $\hat{k}_n$ and $\hat{k}_s$, the upper limits of the equilibrium and saturation ranges, respectively. Shaded bars in panel (b) correspond to values of $\hat{k}_n$ (r in their nomenclature) obtained by Lenain and Melville (2017). The shaded rectangles correspond to the interdecile angular width of $\tau_{br}(\theta)$ as shown in Figure 13b.

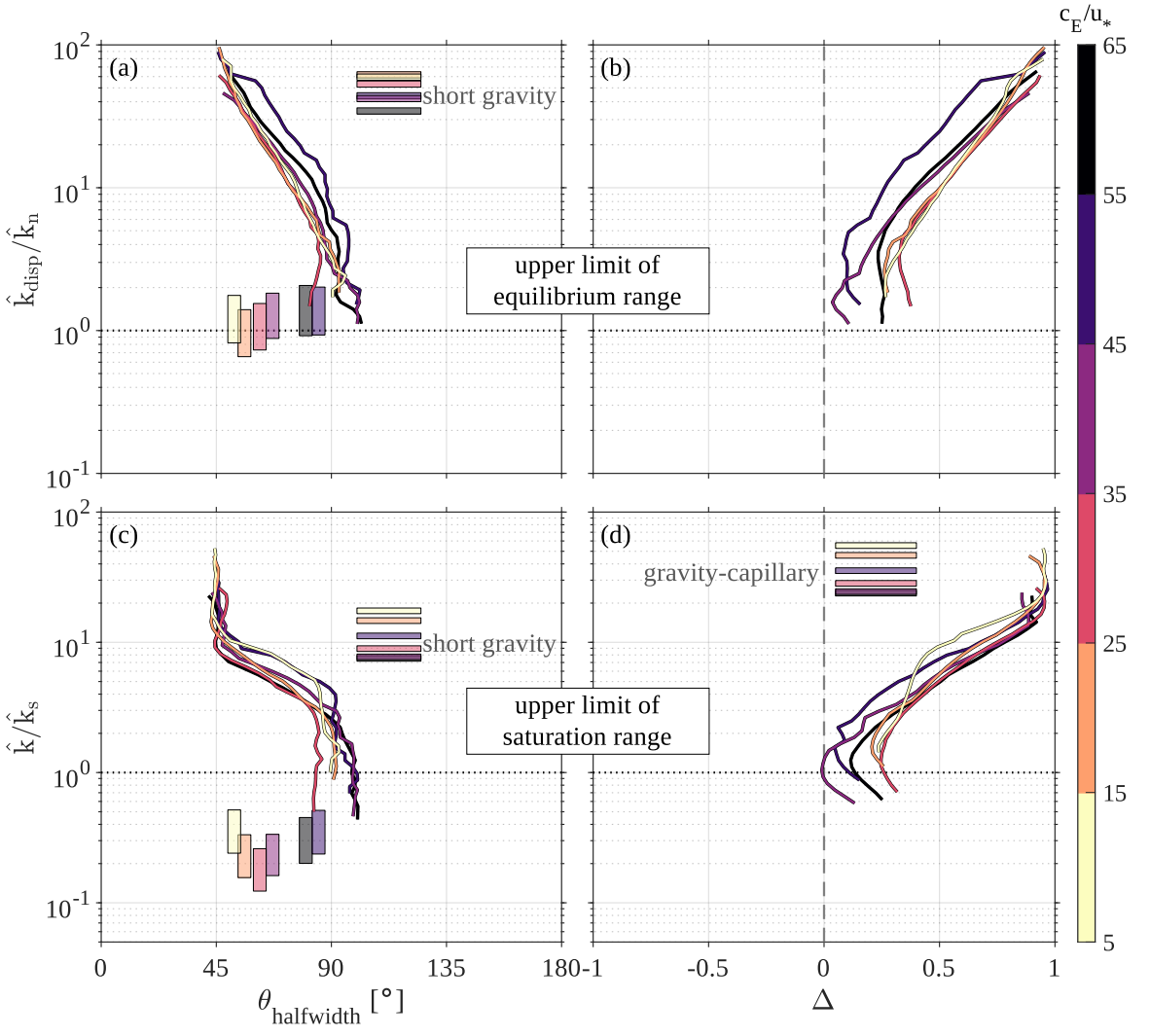

595 FIG. 17. Directional spreading information provided in Figure 16, normalized by transition wavenumbers $\hat{k}_n$
596 and $\hat{k}_s$ as appropriate. The horizontal dashed lines in panels (a-b) and (c-d) correspond to the upper limits of the
597 equilibrium and saturation ranges, respectively.

6. Discussion

The mean directions of short gravity and gravity-capillary (centimeter to decimeter) waves do not appear to be associated with wind-dominant wave misalignment (Figure 15); this fits our intuition that short waves with growth/relaxation timescales of order 10 s and shorter are most responsive to the instantaneous wind (Zappa et al. 2019) and should therefore simply propagate downwind. We note that there is fairly substantial run-to-run offwind variation in mean direction at those short scales (Figure 15c-d). Numerous potential explanations exist for this variability, though two are most likely: short-timescale transience in the wind forcing (direction or magnitude) and influence of off-wind current. In contrast, off-wind propagation of the relatively longer wind waves in the equilibrium and saturation ranges is expected to be the result of *slow* nonstationarity in wind forcing or weakly nonlinear interaction between long waves and windsea. The sign of the predominant misalignment (negative, so waves tend to propagate to the left of the local wind direction) is almost certainly not a general result, but is instead contingent upon the prevailing wind and wave directions during the period of observation (Figure 3), with long waves subject to refraction on the continental shelf. Nevertheless, general conclusions may be drawn from the behavior of wind waves which are sufficiently short to be considered as "deep water" waves (at this site of 15 m mean depth, $f > 0.21$ Hz); this criterion encompasses the entirety of the equilibrium range (and shorter) waves considered here (Figure 7). Consistent with the deep water results of Thomson et al. (2013), Voermans et al. (2020) found that waves in the equilibrium range tend to propagate downwind. However, the variation about this mean (20°-60° RMSE) is substantial enough to merit further investigation into the causes of off-wind wave propagation in the equilibrium range– including impacts related to windsea-long wave interaction.

Our independent (i.e., not determined via polarimetric slope sensing) measurements of breaking waves determined that air-entraining breakers tend to orient in the direction of waves in the equilibrium and saturation ranges; the breaker wavelengths inferred from c_{br} via small-amplitude wave theory place them as straddling the transition between these two ranges (Figure 17). This result is consistent with the expectation that wave spectral energy density in the equilibrium and saturation ranges is determined by a balance between processes, the predominant sink of which is dissipation due to wave breaking. As shown in Figure 14, breaking fronts in older seas are more readily steered off the wind direction by long waves than they might be in younger seas. Given the

importance of breaking waves in near-surface Lagrangian drift (Pizzo et al. 2019), it is somewhat surprising that the direction of near-surface current does not appear to be reliably impacted by off-wind breaker propagation (Figure 15f). It may be that direct (viscous) wind forcing of surface drift is dominant in older seas, where breaking fronts are observed to have the greatest off-wind deflection. We note that the measurement intervals and quality control criteria differ between the skin velocity and wave breaking datasets, so this particular disparity is the most difficult to resolve given the present dataset.

The conditions under which essential wave parameters will become uncoupled from wind forcing is of particular interest to this study. Sticking with the somewhat crude parameter of omnidirectional wave age c_E/u_*, we see evidence for a transition from tightly wind-coupled to weakly wind-coupled around $c_E/u_* \approx 40$. To be specific, the equilibrium-saturation transition wavenumber shows no average response to changes in wave age (but demonstrates substantially-elevated variation) beyond $c_E/u_* \approx 40$ (Figure 9a). This scale (k_n) appears connected to the breaker momentum flux-weighted average wavenumber k_{br} for all wave ages (Figure 17a). However, as demonstrated in Figure 13, the breaking fronts for younger seas ($c_E/u_* < 45$) are more tightly spread about the mean direction. This finding of an approximate transition point in tight wind/wave coupling is not confined to the present study (cf. Sutherland and Melville (2013), in particular the analogous decoupling of breaking momentum flux with wind stress shown in Figure 5; also– variation of normalized surface roughness with wave age shown in Figure 5 of Drennan et al. (2003)). We suspect that a substantial shift in breaking frequency (incidence) is occurring for $c_E/u_* > 40$, beyond which breaking events are loosely coupled to the local wind forcing. This interpretation is consistent with the finding of Gemmrich and Farmer (1999) that breaking frequency exhibits an extreme (step-like) response to wave age (a response that is also contingent upon fetch and location).

Mean wave directional propagation tells only one part of the story; it is essential to also describe the spreading and modality of wave spectra. We note that we are not able to fully characterize wavenumber-directional spreading in the equilibrium range or near the wave spectral peak; this precludes estimation of the nonlinear wave-wave interaction source term (e.g., via the optimized WRT (Webb-Resio-Tracy) method as implemented by van Vledder (2006)). As such, the present analysis should be considered complementary to those which directly resolve equilibrium wave directional spreading (Romero et al. 2012; Leckler et al. 2015; Lenain and Melville 2017, e.g.).

This composite approach is not unusual: for example, the classic Airborne Topographic Mapper observations described in Romero and Melville (2010) and Romero et al. (2012) resolved the surface wave directional spectrum up to $k_{Nyq} = 0.35$ rad m^{-1}, beyond which fixed LiDAR was required for inferring the upper limit of the saturation spectrum. The "sweet spot" of our wavenumber-directional observations spans the short gravity and gravity-capillary regimes. The simultaneous narrowing of directional spread and the sea's tendency towards unimodality with increasing wavenumber at those scales is both revealing (these are the first systematic field observations of such behavior) and obvious (we expect very short wind waves to propagate downwind). A reasonable explanation for this behavior: wind input of wave action is preferentially downwind (growth rate $\beta \sim (u_*/c)^2\omega \cos(\theta - \theta_{wind})$, Plant (1982)) while viscous dissipation is omnidirectional and strongly scale-dependent (relaxation rate $\beta_\nu \sim 4\nu k^2$, Donelan and Plant (2009)). At these short (λ of order 1 cm) scales, wind input is dominant.

A Brief Discussion Regarding Sample Size

As stated in section 3, our wind-wave analysis rests on 56 individual measurements. This sample size is modest when compared to datasets built from persistent sensing systems like buoys or wave staffs. However, it is the largest of its kind when one considers the range of surface wave scales resolved (down to sub-centimeter in wavelength) in tandem with breaking wave and near-surface current observations. The size of the dataset and the breadth of its parameter space for key variables (e.g. wind forcing, wind-wave misalignment) appears to be sufficient for adequately describing first-order effects– that is, variation of the wave spectrum with wind speed, as in Figures 6 & 7. In order to go a step further and investigate the variation of first-order properties (e.g., wind wave direction) with respect to wind-long wave misalignment, we performed wind forcing-agnostic regressional analysis (Figure 15). A more full description of the variation of first-order properties with respect to wind-wave misalignment might require conditional analysis which would split the dataset and diminish statistical power (Montgomery 2017). The large residual case-to-case variations in the mean wind-relative propagation direction of short gravity and gravity-capillary waves (Figure 15) might well be connected to third-order effects (e.g. transience in wind forcing, nonlinear wave effects) by conditional analysis of a dataset with sufficiently large size. We performed a basic power analysis (Montgomery 2017) with conservative assumptions: we estimate $N = 107$ for effect size

(Cohen's d, or standard deviation-normalized difference) of 0.2, statistical power ($1-\beta$, where β is the false negative rate) of 0.8, and significance threshold (α, or false positive rate) of 0.005. That is– in order to detect a fairly small effect which causes the mean of one group to differ from that of the other by 1/5 standard deviations, with no greater than 1/200 chance that the difference is attributable to random variation, with no greater than a 20% likelihood of failing to detect a true effect, we require at least 107 samples *per group*. If we wish to investigate the mechanisms by which very short waves or near-surface current become misaligned with the local wind direction, we would need $N \geq 107$ cases in which we observe the particular phenomenon we are testing (e.g., rising/falling/veering wind). Depending on the phenomenon of interest, this might require $N \approx 500$ (or greater) individual QC-passed short wave observations to ensure that sufficient cases are collected– a number approximately one order of magnitude larger than the dataset considered in the present analysis. We hope that recent advancements in the processing and interpretation of sea surface polarimetry (Laxague et al. 2025a,b) reduce the barrier to entry enough to allow for both broader adoption of the technique and a substantial uplift in dataset sizes.

7. Summary

This study was motivated by a desire to better understand wind-wave directionality over a wide range of scales. The observational effort which was performed in service of this goal yielded a multi-month observational campaign in which wind stress, the directional wave spectrum, the directional breaking crest length distribution, and various other useful environmental parameters (e.g., near-surface current) were obtained. As we stated in section 1, there is particular value in parsing our results by the spatial/temporal scale of the surface waves we observed. We elected to use wave regimes defined either by (1) the particular sources and sinks in the wave action balance (equilibrium, saturation) or by (2) the dominant restoring force for waves of a particular scale (short gravity, gravity-capillary). Our quantification of breaking wave characteristics (including momentum flux, mean direction, and directional spread) allowed for the inclusion of breakers in our analysis (Hogan et al. 2025). Infrared observations of the thermal skin advection provided a supplementary measure of the true surface current velocity (Liu et al. 2025).

We offer a condensed summary of the key findings:

- The scale of transition from saturation to equilibrium range varies with wave age in a manner that is consistent with prior field observations Romero and Melville (2010) and is well-described by the previously-established parametric relationship of Hwang and Wang (2001).
- Misalignment between long waves and the local wind forcing is associated with off-wind propagation of waves in the equilibrium and saturation spectral subranges (as well as breaking wave fronts).
- Waves in the short gravity and gravity-capillary subranges and very near-surface current exhibit variability in mean direction with respect to the wind, but that variation is not associated with long wave-wind misalignment.
- Breaking wave fronts are found to move at speeds which place them near the transition between the equilibrium and saturation spectral subranges. For seas older than $c_E/u_* \approx 35$, breaking front coupling to wind weakens and the directional spread broadens substantially.
- Directional spreading peaks at the upper limit of the saturation range; the sea narrows and becomes unimodal for short gravity and gravity-capillary waves. This behavior is owed to the nature of the balance between wind input and viscous dissipation at those short scales.

We suspect that some of the residual variability in mean directional misalignment between wind, current, and waves (or scale-dependent directionality of the latter) may be attributed to transience in wind or nonlinear wave-wave interactions. However, the sample size of the present combined data set is approximately one order of magnitude too small to definitively resolve such higher-order effects. Nevertheless, our first-order characterizations of the observations (e.g., scale-dependent directional steering by long waves, the wave age of breaker decoupling from wind forcing, and the spreading/modality transition from the saturation range to gravity-capillary waves) are robust. An expanded future deployment in this style is likely to enable the conditional analysis requried for elucidation of higher-order processes which impact wind-wave-current coupling.

Acknowledgments. The authors are grateful for the efforts of Steve Faluotico, Jay Sisson, and the crew of the *R/V Tioga*. Field observations would not have been possible without the efforts of Carson Witte and Suki Wong. Initial data collection was supported by awards 17-56789 (ACL) and 17-56839 (CJZ) from NSF, award N00014-22-1-2183 from ONR (CJZ), and award 80NSSC19K1397 from NASA (CJZ). Data analysis was supported by NSF awards 20-49578 (NJML) & 20-49579 (CJZ). NJML also gratefully acknowledges NSF award 23-40712. J-VB was supported by Met Norway (FUNDING SOURCE?).

Data availability statement. The full surface slope field dataset is publicly available at NASA PO.DAAC (`https://podaac.jpl.nasa.gov/`); DOI: 10.5067/SMODE-WSLOPE. Intermediate products (wavenumber and frequency directional spectra) are available at `https://zenodo.org/records/17388349`. Additional data and codes specific to the production of figures in this manuscript are available through GitHub: `https://github.com/unh-cassll/wind-wave-directionality-paper`. All codes used in the preliminary stages of processing are also available through GitHub: `https://github.com/unh-cassll/polarimetric-slope-sensing` (polarimetric slope sensing); `https://github.com/unh-cassll/wave-slope-spectral-analysis` (wave spectral analysis).

APPENDIX A

Vertical Profile of Wind Speed and Wind Stress

From mid-October 2019 to early February 2020, all five 3D sonic anemometers on ASIT operated with high uptime. The mean profiles (binned by ten-meter wind speed U_{10}) are shown in Figure A1. Cases with non-stationary wind velocities or misalignment between the sonic anemometer orientation and wind velocity vector ($|\Delta\theta| > 90°$) were excluded from all analyses.

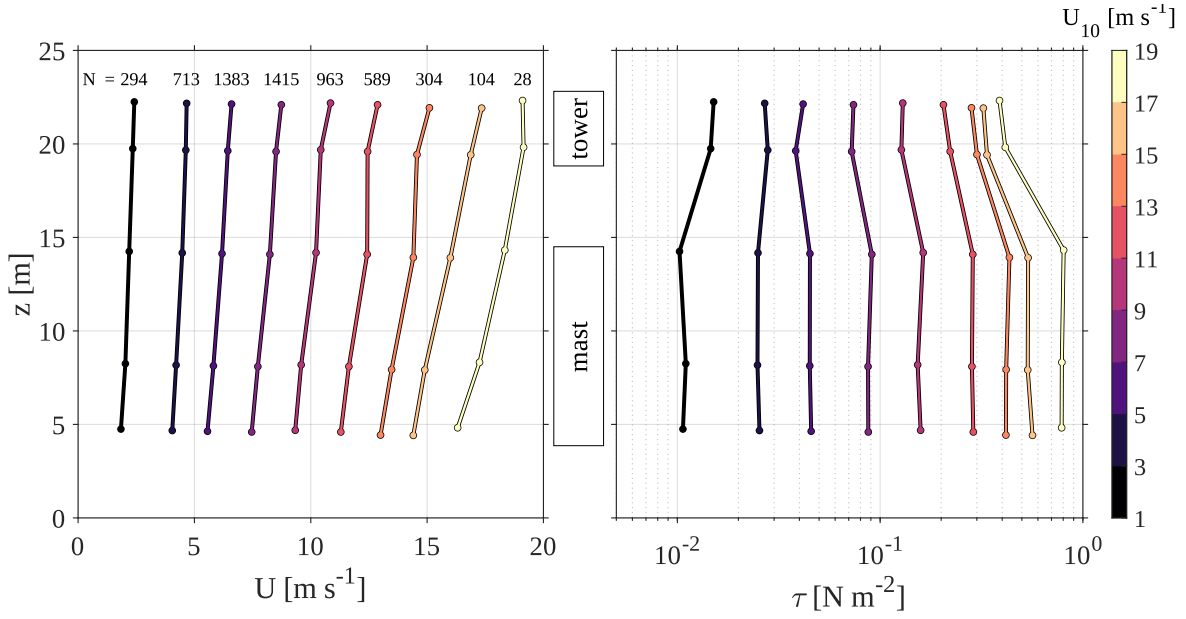

FIG. A1. Vertical profiles of wind speed (left) and wind stress magnitude (right) over the full ASIT2019 field campaign, bin-averaged according to the limits specified in the colorbar. The number of individual 20-minute measurements per bin are marked above the wind speed profiles in the left panel. The location of each anemometer (e.g., mast or tower) is indicated by the text labels between the two panels.

APPENDIX B

Calculation of the Wavenumber-Frequency Directional Slope Spectrum

Given a series of measurements of two orthogonal components of the water surface slope field

$$\nabla\eta(x,y,t) = \left[\mathcal{S}_x(x,y,t)\mathbf{x} + \mathcal{S}_y(x,y,t)\mathbf{y}\right] \tag{B1}$$

We compute the wavenumber-frequency directional slope spectrum in Cartesian coordinates:

$$S(k_x, k_y, \omega) = \frac{\mathcal{A}_x^* \mathcal{A}_x + \mathcal{A}_y^* \mathcal{A}_y}{0.5 N^2 \Delta k^2 \Delta \omega} \tag{B2}$$

... where $\mathcal{A}_i = \mathcal{F}\{\mathcal{S}_i\}$ is the Fourier transform of a slope field component array, N is the total number of points in the array, Δk & $\Delta\omega$ are the wavenumber & frequency increments, and * denotes complex conjugation. S is the variance density spectrum, so

$$\langle \mathcal{S}^2 \rangle = \iiint S(k_x, k_y, \omega) \mathrm{d}k_x \mathrm{d}k_y \mathrm{d}\omega \tag{B3}$$

$$= \iiint S(k, \omega, \theta) k \mathrm{d}k \mathrm{d}\theta \mathrm{d}\omega \tag{B4}$$

... where $\langle \mathcal{S}^2 \rangle = \langle \mathcal{S}_x^2 \rangle + \langle \mathcal{S}_y^2 \rangle$ is the total slope variance (or mean square slope). In order to obtain $S(k, \omega, \theta)$, we perform a Cartesian to polar coordinate transformation of the wavenumber directional spectrum $S(k_x, k_y) \rightarrow S(k, \theta)$ at each frequency slice, ensuring that wave slope variance is conserved in the process.

In Figure B1 we show that approximately 80% of the wave scales resolved in the spatial domain have not been shown in the example graphics leading up to this point. This wastefulness is necessitated by our low temporal resolution (1/30 s) relative to the spatial resolution of our slope measurement ($\approx$1 cm), which limits the maximum wavenumber at which we are able to obtain unambiguous directional wave information. However, we were able to retrieve the mean propagation direction of gravity-capillary waves ($k > 117$ rad m^{-1}) by applying a mask to exclude spectral features more than 90° off the mean short gravity wave direction.

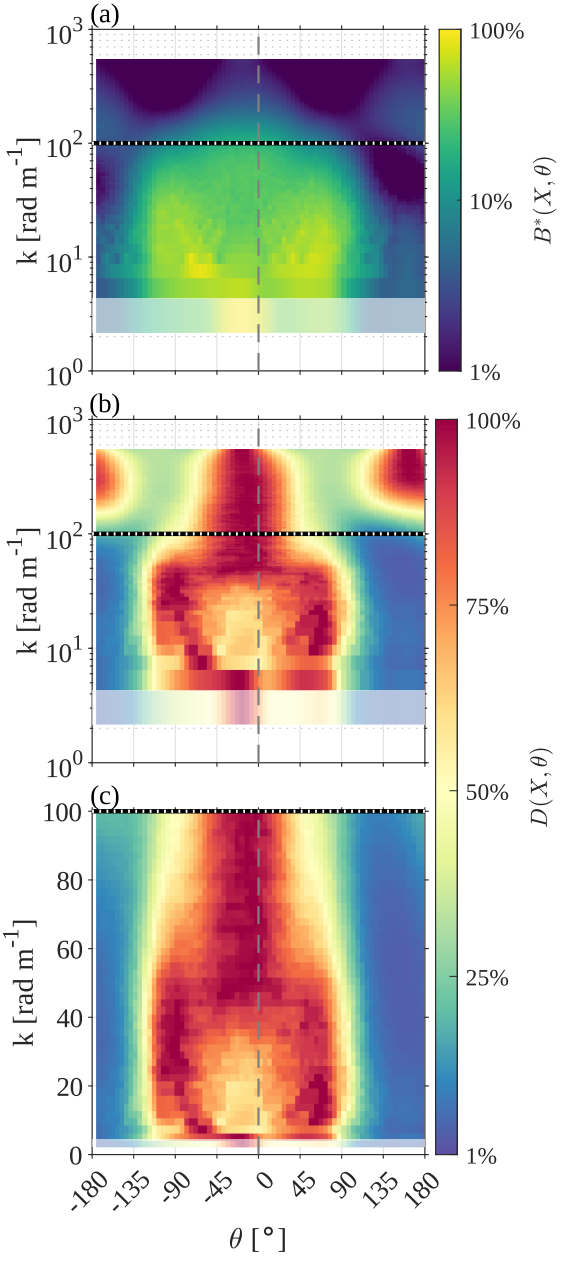

FIG. B1. Extended view of directional spectrum shown in Figure 10. (a) Example wavenumber-directional saturation spectrum. Corresponding directional spreading function D is shown over (b) the full wavenumber range and (c) the truncated range $k \in [6.45, 100]$ rad m^{-1}, as used throughout the directional spectra figures presented in the main text.

APPENDIX C

Definitions of Spectral Subranges

The wavenumber-directional and frequency-directional spectra of surface gravity waves tend to follow a set of well-known power laws in the equilibrium and saturation ranges (Phillips 1985):

$$\text{eq.} \begin{Bmatrix} F_k(k,\theta) \propto k^{-3.5} \\ F_\omega(\omega,\theta) \propto \omega^{-4} \end{Bmatrix}, \quad \text{sat.} \begin{Bmatrix} F_k(k,\theta) \propto k^{-4} \\ F_\omega(\omega,\theta) \propto \omega^{-5} \end{Bmatrix} \tag{C1}$$

In this section, we use the convention of Phillips and Kitaigorodskii in reporting the wave radian frequency ω rather than the cyclic frequency f (used elsewhere in the manuscript, as seen in Figure C1). Given a relationship in terms of one independent variable (e.g., ω), the relationship dependence with respect to the second independent variable (e.g., k) may be determined through conservation of energy:

$$\iint F_k(k,\theta) k \mathrm{d}k \mathrm{d}\theta = \iint F_\omega(\omega,\theta) \mathrm{d}\omega \mathrm{d}\theta \tag{C2}$$

...and the assumption that the dispersion relation $\Omega \equiv \Omega(k)$ is isotropic (Kitaigordskii et al. 1975; Kitaigorodskii 1983):

$$F_\omega(\omega,\theta) = \left. \frac{k F_k(k,\theta)}{\frac{\partial \Omega}{\partial k}} \right|_{k=\omega^2/g} \tag{C3}$$

Note that the omnidirectional wavenumber spectral shape goes as kF_k: $k^{-2.5}$ and k^{-3} for the equilibrium and saturation ranges, respectively.

Given these definitions, we systematically identified the frequency and wavenumber extrema of the wave spectra equilibrium and saturation ranges. First, a concatenated long wave / short wave (E-PSS / direct) omnidirectional frequency spectrum was computed for each acquisition and resampled onto a logarithmically-spaced frequency vector ranging from 0.05 to 5 Hz in 64 increments. Then, a moving-window (16 sample) least-squares linear regression was computed for the base-ten logarithms of the independent Fourier variable and the spectral energy density. The lower extremum of the equilibrium range was defined as the last index for which the regression slope (minus the 95% confidence interval) n such that $B(f) \sim f^5 F(f) \propto f^n$ exceeded 1. Analogous thresholds were set for the equilibrium-saturation transition ($n = 0$) and the upper limit of the saturation range ($n = -0.25$). As demonstrated in Figure C2, this fact can be exploited to identify

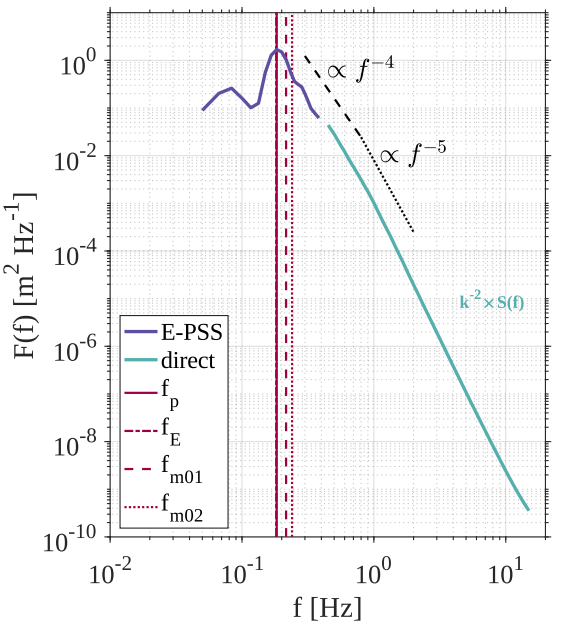

Fig. C1. Example omnidirectional frequency spectrum. The teal trace corresponds to the "direct" spectrum obtained from the wavenumber-frequency directional spectrum while the violet trace corresponds to long wave spectrum inferred via E-PSS (Laxague et al. 2025b). Red lines correspond to peak/mean wave frequencies computed from the spectra: peak frequency $f_p = 0.183$ Hz, energy-weighted mean frequency $f_E = 0.175$ Hz, significant wave frequency $f_{m01} = 0.216$ Hz, and mean wave frequency $f_{m02} = 0.242$ Hz. These frequencies correspond to the following celerities: $c_p = 8.26$ m s^{-1}, $c_E = 8.55$ m s^{-1}, $c_{m01} = 7.17$ m s^{-1}, $c_{m02} = 6.45$ m s^{-1},

the extrema of the spectral subranges of interest. As explained in section 5, the limits of the short gravity and gravity-capillary regimes are fixed in wavenumber space as determined by the Bond number $Bo \equiv \frac{\Delta\rho g}{\sigma k^2}$.

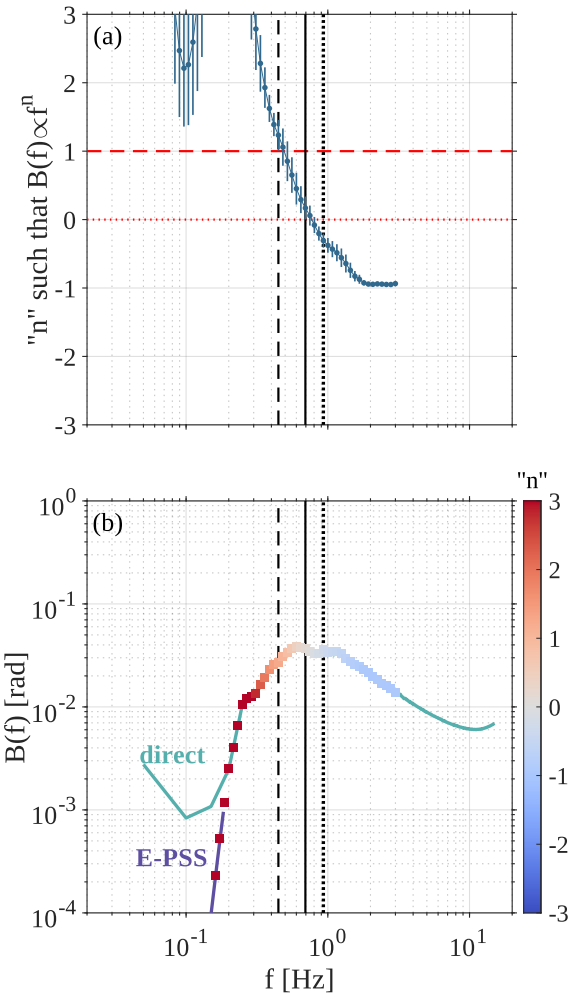

FIG. C2. (a) Frequency saturation spectral slope "n" determined from least-squares linear regressions in log-log space, with vertical bars indicating the 95% confidence intervals of the slope estimates. Horizontal dashed and solid red lines correspond to the canonical equilibrium and saturation range slopes, respectively. (b) Frequency saturation spectrum, with color indicating local slope "n". In both panels, the vertical lines mark the inferred subrange limits: start of equilibrium (dashed), transition from equilibrium to saturation (solid), end of saturation (dotted).

References

Ayet, A., and B. Chapron, 2022: The Dynamical Coupling of Wind-Waves and Atmospheric Turbulence: A Review of Theoretical and Phenomenological Models. *Boundary-Layer Meteorology*, **183 (1)**, 1–33, https://doi.org/10.1007/s10546-021-00666-6.

Ayet, A., B. Chapron, J.-L. Redelsperger, G. Lapeyre, and L. Marié, 2020: On the Impact of Long Wind-Waves on Near-Surface Turbulence and Momentum Fluxes. *Boundary-Layer Meteorology*, **174 (3)**, 465–491, https://doi.org/10.1007/s10546-019-00492-x.

Banner, M. L., 1990: Equilibrium Spectra of Wind Waves. *Journal of Physical Oceanography*, **20 (7)**, 966–984, https://doi.org/10.1175/1520-0485(1990)020⟨0966:ESOWW⟩2.0.CO;2.

Banner, M. L., I. S. F. Jones, and J. C. Trinder, 1989: Wavenumber spectra of short gravity waves. *Journal of Fluid Mechanics*, **198 (1989)**, 321–344, https://doi.org/10.1017/S0022112089000157.

Banner, M. L., and W. K. Melville, 1976: On the separation of air flow over water waves. *Journal of Fluid Mechanics*, **77 (4)**, 825–842, https://doi.org/10.1017/S0022112076002905.

Benetazzo, A., 2006: Measurements of short water waves using stereo matched image sequences. *Coastal Engineering*, **53 (12)**, 1013–1032, https://doi.org/10.1016/J.COASTALENG.2006.06.012.

Bergamasco, F., A. Torsello, M. Sclavo, F. Barbariol, and A. Benetazzo, 2017: WASS: An open-source pipeline for 3D stereo reconstruction of ocean waves. *Computers & Geosciences*, **107**, 28–36, https://doi.org/10.1016/j.cageo.2017.07.001.

Björkqvist, J.-V., H. Pettersson, W. M. Drennan, and K. K. Kahma, 2019: A New Inverse Phase Speed Spectrum of Nonlinear Gravity Wind Waves. *Journal of Geophysical Research: Oceans*, **124 (8)**, 6097–6119, https://doi.org/10.1029/2018jc014904.

Caulliez, G., and C.-A. Guérin, 2012: Higher-order statistical analysis of short wind wave fields. *Journal of Geophysical Research*, **117 (C6)**, n/a–n/a, https://doi.org/10.1029/2011JC007854.

Chang, Y., A. Kirincich, and J. B. Edson, 2025: Observations of Coastal Wind Momentum Flux: Dependence on Fetch and Waves with Comparisons to COARE. *Journal of Physical Oceanography*, **55 (9)**, 1321–1334, https://doi.org/10.1175/JPO-D-24-0242.1.

Cifuentes-Lorenzen, A., C. J. Zappa, J. B. Edson, J. O'Donnell, and D. S. Ullman, 2024: Exploring the Role of Wave-Driven Turbulence at the Air-Sea Interface Through Measurements of TKE Dissipation Rates Across the Air-Sea Interface. *Journal of Geophysical Research: Oceans*, **129 (8)**, e2023JC020 308, https://doi.org/10.1029/2023JC020308.

Denny, J., W. Danforth, D. Foster, and C. Sherwood, 2008: USGS Open-File Report 2008-1288: Geophysical Data Collected off the South Shore of Martha's Vineyard, Massachusetts. URL https://pubs.usgs.gov/of/2008/1288/.

Donelan, M. A., and W. J. Plant, 2009: A threshold for wind-wave growth. *Journal of Geophysical Research*, **114 (7)**, 1–8, https://doi.org/10.1029/2008JC005238.

Drazen, D. A., W. K. Melville, and L. Lenain, 2008: Inertial scaling of dissipation in unsteady breaking waves. *Journal of Fluid Mechanics*, **611**, 307–332, https://doi.org/10.1017/S0022112008002826.

Drennan, W. M., H. C. Graber, and M. A. Donelan, 1999: Evidence for the effects of swell and unsteady winds on marine wind stress. *Journal of Physical Oceanography*, **29 (8 PART 1)**, 1853–1864, https://doi.org/10.1175/1520-0485(1999)029⟨1853:EFTEOS⟩2.0.CO;2.

Drennan, W. M., H. C. Graber, D. Hauser, and C. Quentin, 2003: On the wave age dependence of wind stress over pure wind seas. *Journal of Geophysical Research: Oceans*, **108 (C3)**, https://doi.org/10.1029/2000JC000715.

Duncan, J. H., 1981: An experimental investigation of breaking waves produced by a towed hydrofoil. *Proceedings of the Royal Society of London. A. Mathematical and Physical Sciences*, **377 (1770)**, 331–348, https://doi.org/10.1098/rspa.1981.0127.

Duncan, J. H., 1983: The breaking and non-breaking wave resistance of a two-dimensional hydrofoil. *Journal of Fluid Mechanics*, **126**, 507–520, https://doi.org/10.1017/S0022112083000294.

Edson, J. B., and Coauthors, 2007: The Coupled Boundary Layers and Air–Sea Transfer Experiment in Low Winds. *Bulletin of the American Meteorological Society*, **88 (3)**, 341 – 356, https://doi.org/10.1175/BAMS-88-3-341.

Elfouhaily, T., B. Chapron, K. B. Katsaros, and D. C. Vandemark, 1997: A unified directional spectrum for long and short wind-driven waves. *Journal of Geophysical Research*, **102 (C7)**, 15 781–15 796, https://doi.org/10.1029/97JC00467.

Fisher, A. W., L. P. Sanford, M. E. Scully, and S. E. Suttles, 2017: Surface Wave Effects on the Translation of Wind Stress across the Air–Sea Interface in a Fetch-Limited, Coastal Embayment. *Journal of Physical Oceanography*, **47 (8)**, 1921–1939, https://doi.org/10.1175/JPO-D-16-0146.1.

Gemmrich, J. R., and D. M. Farmer, 1999: Observations of the Scale and Occurrence of Breaking Surface Waves. *Journal of Physical Oceanography*, **29 (10)**, 2595–2606, https://doi.org/10.1175/1520-0485(1999)029⟨2595:OOTSAO⟩2.0.CO;2.

Hager, W. H., 2012: Wilfrid Noel Bond and the Bond number. *Journal of Hydraulic Research*, **50 (1)**, 3–9, https://doi.org/10.1080/00221686.2011.649839.

Hara, T., and S. E. Belcher, 2002: Wind forcing in the equilibrium range of wind-wave spectra. *Journal of Fluid Mechanics*, **470**, 223–245, https://doi.org/10.1017/S0022112002001945.

Hogan, L., C. J. Zappa, A. Cifuentes-Lorenzen, J. B. Edson, J. O'Donnell, and D. S. Ullman, 2025: Observations of Breaking Wave Dissipation and Their Relationship to Atmosphere-Ocean Energy Transfer. *Journal of Geophysical Research: Oceans*, **130 (6)**, e2024JC022 130, https://doi.org/10.1029/2024JC022130.

Husain, N. T., T. Hara, and P. P. Sullivan, 2022a: Wind Turbulence over Misaligned Surface Waves and Air–Sea Momentum Flux. Part I: Waves Following and Opposing Wind. *Journal of Physical Oceanography*, **52 (1)**, 119 – 139, https://doi.org/10.1175/JPO-D-21-0043.1.

Husain, N. T., T. Hara, and P. P. Sullivan, 2022b: Wind Turbulence over Misaligned Surface Waves and Air–Sea Momentum Flux. Part II: Waves in Oblique Wind. *Journal of Physical Oceanography*, **52 (1)**, 141 – 159, https://doi.org/10.1175/JPO-D-21-0044.1.

Hwang, P. A., 2005: Wave number spectrum and mean square slope of intermediate-scale ocean surface waves. *Journal of Geophysical Research*, **110 (10)**, 1–7, https://doi.org/10.1029/2005JC003002.

Hwang, P. A., and D. W. Wang, 2001: Directional Distributions and Mean Square Slopes in the Equilibrium and Saturation Ranges of the Wave Spectrum. *Journal of Physical Oceanography*, **31 (5)**, 1346–1360, https://doi.org/10.1175/1520-0485(2001)031⟨1346:DDAMSS⟩2.0.CO;2.

Janssen, P. a. E. M., 1991: Quasi-linear Theory of Wind-Wave Generation Applied to Wave Forecasting. *Journal of Physical Oceanography*, **21 (11)**, 1631–1642, https://doi.org/10.1175/1520-0485(1991)021⟨1631:QLTOWW⟩2.0.CO;2.

Kahma, K. K., M. A. Donelan, W. M. Drennan, and E. A. Terray, 2016: Evidence of Energy and Momentum Flux from Swell to Wind. *Journal of Physical Oceanography*, **46 (7)**, 2143–2156, https://doi.org/10.1175/JPO-D-15-0213.1.

Kitaigordskii, S. A., V. P. Krasitskii, and M. M. Zaslavskii, 1975: On Phillips' Theory of Equilibrium Range in the Spectra of Wind-Generated Gravity Waves. *Journal of Physical Oceanography*, **5 (3)**, 410–420, https://doi.org/10.1175/1520-0485(1975)005⟨0410:OPTOER⟩2.0.CO;2.

Kitaigorodskii, S. A., 1983: On the Theory of the Equilibrium Range in the Spectrum of Wind-Generated Gravity Waves. *Journal of Physical Oceanography*, **13 (5)**, 816–827, https://doi.org/10.1175/1520-0485(1983)013⟨0816:OTTOTE⟩2.0.CO;2.

Laxague, N. J. M., M. Curcic, J.-V. Björkqvist, and B. K. Haus, 2017a: Gravity-capillary wave spectral modulation by gravity waves. *IEEE Transactions on Geoscience and Remote Sensing*, **55 (5)**, https://doi.org/10.1109/TGRS.2016.2645539.

Laxague, N. J. M., Z. G. Duvarcı, L. Hogan, S. P. Anderson, and C. J. Zappa, 2025a: The Effects of Subpixel Variability on Polarimetric Sensing of Ocean Waves. *IEEE Transactions on Geoscience and Remote Sensing*, **63**, 1–13, https://doi.org/10.1109/TGRS.2025.3538460.

Laxague, N. J. M., Z. G. Duvarcı, L. Hogan, J. Liu, C. Bouillon, and C. J. Zappa, 2025b: E-PSS: the Extended Polarimetric Slope Sensing technique for measuring ocean surface waves. *IEEE Journal of Selected Topics in Applied Earth Observations and Remote Sensing*.

930 Laxague, N. J. M., B. K. Haus, D. J. Bogucki, and T. M. Özgökmen, 2015: Spectral characterization
931 of fine-scale wind waves using shipboard optical polarimetry. *Journal of Geophysical Research*,
932 **120 (4)**, https://doi.org/10.1002/2014JC010403.

933 Laxague, N. J. M., B. K. Haus, D. G. Ortiz-Suslow, C. J. Smith, G. Novelli, H. Dai, T. M. Özgökmen,
934 and H. C. Graber, 2017b: Passive optical sensing of the near-surface wind-driven current
935 profile. *Journal of Atmospheric and Oceanic Technology*, **34 (5)**, 1097–1111, https://doi.org/
936 10.1175/JTECH-D-16-0090.1.

937 Laxague, N. J. M., and C. J. Zappa, 2020a: The impact of rain on ocean surface waves
938 and currents. *Geophysical Research Letters*, **47 (7)**, e2020GL087 287, https://doi.org/10.1029/
939 2020GL087287.

940 Laxague, N. J. M., and C. J. Zappa, 2020b: Observations of mean and wave orbital flows in the
941 ocean's upper centimetres. *Journal of Fluid Mechanics*, **887**, A10, https://doi.org/10.1017/jfm.
942 2019.1019.

943 Laxague, N. J. M., C. J. Zappa, D. A. LeBel, and M. L. Banner, 2018a: Spectral characteristics
944 of gravity-capillary waves, with connections to wave growth and microbreaking. *Journal of*
945 *Geophysical Research: Oceans*, **123 (7)**, https://doi.org/10.1029/2018JC013859.

946 Laxague, N. J. M., C. J. Zappa, S. Soumya, and O. Wurl, 2024: The suppression of ocean waves
947 by biogenic slicks. *Journal of The Royal Society Interface*, **21 (220)**, 20240 385, https://doi.org/
948 10.1098/rsif.2024.0385.

949 Laxague, N. J. M., and Coauthors, 2018b: Observations of Near-Surface Current Shear Help
950 Describe Oceanic Oil and Plastic Transport. *Geophysical Research Letters*, **45 (1)**, https://doi.org/
951 10.1002/2017GL075891.

952 Leckler, F., F. Ardhuin, C. Peureux, A. Benetazzo, F. Bergamasco, and V. A. Dulov, 2015:
953 Analysis and Interpretation of Frequency-Wavenumber Spectra of Young Wind Waves. *Journal*
954 *of Physical Oceanography*, **45 (10)**, 2484–2496, https://doi.org/10.1175/JPO-D-14-0237.1.

955 Lenain, L., and W. K. Melville, 2017: Measurements of the directional spectrum across the
956 equilibrium-saturation ranges of wind-generated surface waves. *Journal of Physical Oceanog-*
957 *raphy*, **47 (7)**, https://doi.org/10.1175/JPO-D-17-0017.1.

Lin, Z., T. A. A. Adcock, and M. L. McAllister, 2022: Estimating ocean wave directional spreading using wave following buoys: a comparison of experimental buoy and gauge data. *Journal of Ocean Engineering and Marine Energy*, **8 (1)**, 83–97, https://doi.org/10.1007/s40722-021-00218-7.

Liu, J., C. J. Zappa, and N. J. M. Laxague, 2025: Near-surface Ocean Current and its Response to Wind Forcing. *Journal of Geophysical Research: Oceans*.

Makin, V. K., V. N. Kudryavtsev, and C. Mastenbroek, 1995: Drag of the sea surface. *Boundary-Layer Meteorology*, **73 (1-2)**, 159–182, https://doi.org/10.1007/BF00708935.

Manzella, E., T. Hara, and P. P. Sullivan, 2024: Reduction of Drag Coefficient Due To Misaligned Wind-Waves. *Journal of Geophysical Research: Oceans*, **129 (5)**, e2023JC020 593, https://doi.org/10.1029/2023JC020593.

Miles, J. W., 1957: On the generation of surface waves by shear flows. *Journal of Fluid Mechanics*, **3 (2)**, 185–204, https://doi.org/10.1017/S0022112057000567.

Montgomery, D. C., 2017: *Design and Analysis of Experiments*. John Wiley & Sons.

Mueller, J. A., and F. Veron, 2009: Nonlinear formulation of the bulk surface stress over breaking waves: Feedback mechanisms from air-flow separation. *Boundary-Layer Meteorology*, **130 (1)**, 117–134, https://doi.org/10.1007/s10546-008-9334-6.

Ortiz-Suslow, D. G., J. Kalogiros, R. Yamaguchi, and Q. Wang, 2021: An Evaluation of the Constant Flux Layer in the Atmospheric Flow above the Wavy Air-Sea Interface. *Journal of Geophysical Research: Atmospheres*, e2020JD032834, https://doi.org/10.1029/2020JD032834.

Peureux, C., A. Benetazzo, and F. Ardhuin, 2018: Note on the directional properties of meter-scale gravity waves. *Ocean Science*, **14 (1)**, 41–52, https://doi.org/10.5194/os-14-41-2018.

Phillips, O. M., 1985: Spectral and statistical properties of the equilibrium range in wind-generated gravity waves. *Journal of Fluid Mechanics*, **156 (1)**, 505.

Pizzo, N., W. K. Melville, and L. Deike, 2019: Lagrangian Transport by Nonbreaking and Breaking Deep-Water Waves at the Ocean Surface. *Journal of Physical Oceanography*, **49 (4)**, 983–992, https://doi.org/10.1175/JPO-D-18-0227.1.

985 Plant, W. J., 1982: A relationship between wind stress and wave slope. *Journal of Geophysical*
986 *Research*, **87 (C3)**, 1961–1967, https://doi.org/10.1029/JC087iC03p01961.

987 Potter, H., C. O. Collins, and D. G. Ortiz-Suslow, 2022: Pier-Based Measurements of Air-Sea
988 Momentum Fluxes Over Shoaling Waves During DUNEX. *Journal of Geophysical Research:*
989 *Oceans*, **127 (11)**, e2022JC018 801, https://doi.org/10.1029/2022JC018801.

990 Romero, L., 2019: Distribution of Surface Wave Breaking Fronts. *Geophysical Research Letters*,
991 **46 (17-18)**, 10 463–10 474, https://doi.org/10.1029/2019GL083408.

992 Romero, L., and K. Lubana, 2022: On the Bimodality of the Wind-Wave Spectrum: Mean Square
993 Slopes and Azimuthal Overlap Integral. *Journal of Physical Oceanography*, **52 (7)**, 1549–1562,
994 https://doi.org/10.1175/JPO-D-21-0299.1.

995 Romero, L., and W. K. Melville, 2010: Airborne Observations of Fetch-Limited Waves in the
996 Gulf of Tehuantepec. *Journal of Physical Oceanography*, **40 (3)**, 441–465, https://doi.org/
997 10.1175/2009JPO4127.1.

998 Romero, L., W. K. Melville, and J. M. Kleiss, 2012: Spectral Energy Dissipation due to Surface
999 Wave Breaking. *Journal of Physical Oceanography*, **42 (9)**, 1421–1444, https://doi.org/10.1175/
1000 JPO-D-11-072.1.

1001 Sutherland, P., and W. K. Melville, 2013: Field measurements and scaling of ocean surface
1002 wave-breaking statistics. *Geophysical Research Letters*, **40 (12)**, 3074–3079, https://doi.org/
1003 10.1002/grl.50584.

1004 Tamura, H., T. Waseda, Y. Miyazawa, and K. Komatsu, 2008: Current-Induced Modulation of
1005 the Ocean Wave Spectrum and the Role of Nonlinear Energy Transfer. *Journal of Physical*
1006 *Oceanography*, **38 (12)**, 2662–2684, https://doi.org/10.1175/2008JPO4000.1.

1007 Thomson, J., E. A. D'Asaro, M. F. Cronin, W. E. Rogers, R. R. Harcourt, and A. Y. Shcherbina,
1008 2013: Waves and the equilibrium range at Ocean Weather Station P. *Journal of Geophysical*
1009 *Research*, **118 (11)**, 5951–5962, https://doi.org/10.1002/2013JC008837.

1010 van Vledder, G. P., 2006: The WRT method for the computation of non-linear four-wave interactions
1011 in discrete spectral wave models. *Coastal Engineering*, **53 (2)**, 223–242, https://doi.org/10.1016/
1012 j.coastaleng.2005.10.011.

Veron, F., and W. K. Melville, 2001: Experiments on the stability and transition of wind-driven water surfaces. *Journal of Fluid Mechanics*, **446**, 25–65, https://doi.org/DOI:undefined.

Villarreal-Olavarrieta, C. E., F. J. Ocampo-Torres, P. Osuna, and R. E. Mora-Escalante, 2024: Effect of waves on the magnitude and direction of wind stress over the Ocean. *Ocean Modelling*, **191**, 102 420, https://doi.org/10.1016/j.ocemod.2024.102420.

Villas Bôas, A. B., and Coauthors, 2019: Integrated Observations of Global Surface Winds, Currents, and Waves: Requirements and Challenges for the Next Decade. *Frontiers in Marine Science*, **6**.

Voermans, J. J., P. B. Smit, T. T. Janssen, and A. V. Babanin, 2020: Estimating Wind Speed and Direction Using Wave Spectra. *Journal of Geophysical Research: Oceans*, **125 (2)**, e2019JC015 717, https://doi.org/10.1029/2019JC015717.

Zappa, C. J., M. L. Banner, R. P. Morison, S. E. Brumer, C. J. Zappa, M. L. Banner, R. P. Morison, and S. E. Brumer, 2016: On the Variation of the Effective Breaking Strength in Oceanic Sea States. *Journal of Physical Oceanography*, **46 (7)**, 2049–2061, https://doi.org/10.1175/JPO-D-15-0227.1.

Zappa, C. J., M. L. Banner, H. Schultz, A. Corrada-Emmanuel, L. B. Wolff, and J. Yalcin, 2008: Retrieval of short ocean wave slope using polarimetric imaging. *Measurement Science and Technology*, **19 (5)**, 055 503, https://doi.org/10.1088/0957-0233/19/5/055503.

Zappa, C. J., M. L. Banner, H. Schultz, J. R. Gemmrich, R. P. Morison, D. A. Lebel, and T. Dickey, 2012: An overview of sea state conditions and air-sea fluxes during RaDyO. *Journal of Geophysical Research*, **117 (5)**, https://doi.org/10.1029/2011JC007336.

Zappa, C. J., N. J. M. Laxague, S. E. Brumer, and S. P. Anderson, 2019: The Impact of Wind Gusts on the Ocean Thermal Skin Layer. *Geophysical Research Letters*, **46 (20)**, 11 301–11 309, https://doi.org/10.1029/2019gl083687.

Zhang, F. W., W. M. Drennan, B. K. Haus, and H. C. Graber, 2009: On wind-wave-current interactions during the Shoaling Waves Experiment. *Journal of Geophysical Research*, **114 (1)**, 12, https://doi.org/10.1029/2008JC004998.

Zhao, D., and M. Li, 2024: Dependence of drag coefficient on the spectral width of ocean waves. *Journal of Oceanography*, **80 (2)**, 129–143, https://doi.org/10.1007/s10872-023-00712-6.